

REVIEW ARTICLE

Molecular pathology via IR and Raman spectral imaging

Max Diem¹, Antonella Mazur¹, Kathleen Lenau¹, Jen Schubert¹, Ben Bird¹, Miloš Miljković¹, Christoph Krafft^{*,2}, and Jürgen Popp^{2,3}

¹ Laboratory for Spectral Diagnosis (LSpD), Department of Chemistry & Chemical Biology, Northeastern University, Boston, MA 02115, USA

² Institute of Photonic Technology, 07745 Jena, Germany

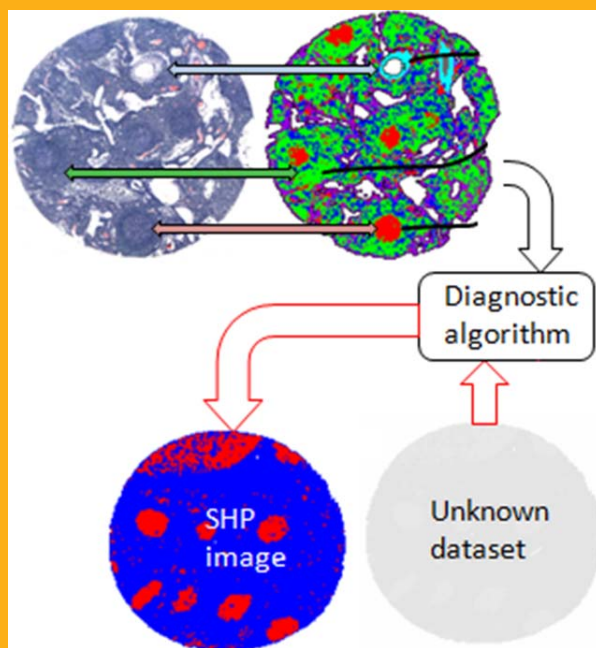
³ Institute of Physical Chemistry and Abbe Center of Photonics, University Jena, 07743 Jena, Germany

Received 15 August 2013, accepted 3 September 2013

Published online 4 November 2013

Key words: IR spectroscopy, Raman spectroscopy, histopathology, cytopathology

During the last 15 years, vibrational spectroscopic methods have been developed that can be viewed as molecular pathology methods that depend on sampling the entire genome, proteome and metabolome of cells and tissues, rather than probing for the presence of selected markers. First, this review introduces the background and fundamentals of the spectroscopies underlying the new methodologies, namely infrared and Raman spectroscopy. Then, results are presented in the context of spectral histopathology of tissues for detection of metastases in lymph nodes, squamous cell carcinoma, adenocarcinomas, brain tumors and brain metastases. Results from spectral cytopathology of cells are discussed for screening of oral and cervical mucosa, and circulating tumor cells. It is concluded that infrared and Raman spectroscopy can complement histopathology and reveal information that is available in classical methods only by costly and time-consuming steps such as immunohistochemistry, polymerase chain reaction or gene arrays. Due to the inherent sensitivity toward changes in the biomolecular composition of different cell and tissue types, vibrational spectroscopy can even provide information that is in some cases superior to that of any one of the conventional techniques.



Schematic of spectral histopathology (SHP) process: diagnostic algorithm is developed by spectral data of well documented specimens and subsequently applied to unknown dataset.

* Corresponding author: e-mail: christoph.krafft@ipht-jena.de

1. Introduction

Histopathology, the microscopic visual inspection of stained tissue sections from biopsies, has been the first line of diagnosis in the treatment of many diseases, in particular cancer. Modern histopathology dates back to the late 19th century, when R. Virchow [1, 2] first used microscopic techniques to gain insight into the changes in cellular morphology that accompany disease. Gross morphological changes that occur with the transition from healthy to diseased tissue include abnormal tissue architecture, the appearance of cells at locations where they are normally not found (metaplasia), the presence of inflammatory cells, abnormal cell morphology including changed nucleus to cytoplasm (N/C) ratio, abnormal nuclear membrane morphology, abnormal chromatin distribution, the number of nucleoli in the nucleus, the presence of unusually large number of mitotic figures indicating rapid cell division, and a plethora of other, often ill-defined features such as foaminess of the cytoplasm, *etc.* [3] To arrive at these diagnostic descriptors, tissue sections, generally about 5 μm thick, are obtained by cutting, *via* a microtome, either formalin-fixed, paraffin embedded tissue blocks, or unfixed, flash-frozen tissue sections. However, in either case, the tissue sections present themselves as white or grayish deposits on microscope slides, and show very little contrast under the microscope. Thus, stains with different affinity for cellular components have been used as early as the late 19th century to create a visual contrast in histopathology. The most common stain in histopathology is the hematoxylin/eosin (H & E) combination stain, [4] which visualizes the basic proteins of the histones (mainly arginine) dark bluish or purple, whereas the eosin imparts a pinkish color to the cytoplasm of cells. We may think of the H & E staining procedure as a very basic “optical method of diagnosis”, since the two stains bind differentially to different cellular structure, making these structures absorb light of different wavelengths, thereby permitting their distinction. Thus, classical histopathology, which uses the human eye as a detector and databases stored in the pathologists mind as a diagnostic discriminator, has been the earliest form of an optical detector to detect disease. A current trend is to shift conventional histopathology towards digital integration [5].

In order to reduce the inter-observer variability of classical histopathology, digital imaging acquisition (at one or more different visible wavelengths) and subsequent computer analysis of the resulting image planes of histopathological specimens have been introduced and commercialized; these methods are generally referred to as “digital pathology” or “whole slide imaging” [6]. However, the analysis of such datasets is still carried out in the “morphology domain”, rather than in the “spectral domain”, since

the few wavelengths at which the images acquired do not permit a true spectral discrimination, and since the images are based on external stains with low inherent discrimination between normal and abnormal structures in tissue.

Although histopathology has been extraordinarily successful as a first line diagnostic tool, modern medicine, especially oncology, requires more than the subjective descriptors available from classical histopathology in order to decide on a suitable treatment regimen for disease. This requirement gave rise to the development of a new methodology which explores the abundance and localization of specific target molecules, such as cancer markers. The most common of these cancer marker-specific techniques is immunohistochemistry (IHC), which was first described in 1942 [7]. This approach is generally described as a method of “molecular pathology”, since it reduces the reliance on morphological features, and instead uses changes in chemical composition – the presence or over-expression of certain marker molecules – as a primary means of distinguishing normal from diseased tissues. In IHC, an optical chromophore – generally a fluorescent label – is attached to a mono- or poly-clonal antibody, to an antigen or other protein marker. Upon binding the antibody-chromophore complex to the target molecules in a cell or tissue, these binding sites can be detected by fluorescence microscopy. IHC has very high sensitivity and specificity, but is restricted by the fact that only markers for which an antibody is applied can produce a detectable signal; i.e., unknown cancer markers cannot be detected in this approach.

Thus, different approaches have been developed, mostly in the biophysical and spectroscopic community. These may be based on detecting either inherent spectral signatures of cellular components or external stains and labels (as discussed above), but are not restricted to the visible wavelengths of light. Miss rates up to 25% have been reported for white light endoscopy that lead to treatment of polyps without malignant potential and, consequently, without benefit but additional costs and risks to the patient [8]. Therefore, fluorescence-based techniques, such as the detection of inherent tissue markers, have gained acceptance mostly in endoscopic diagnoses, and use mostly ultraviolet excitation. Due to the few tissue components that exhibit significant autofluorescence, tissues are often stained with specific fluorophores such as 5-aminolevulinic acid (ALA) [9] or indocyanine green (ICG) [10] to increase sensitivity and specificity, particularly for *in-vivo* observations.

During the last 15 years, methods have been developed that can be viewed as molecular pathology methods that depend on sampling the entire genome, proteome and metabolome of cells and tissues,

rather than probing for the presence of selected markers [11, 12]. These methods rely on the detection of the inherent spectral signatures of the biochemical components in a pixel of tissue. This is possible using vibrational spectroscopy, which comprises two well-established spectroscopic techniques. As the name implies, vibrational spectroscopy monitors the internal motion of atoms in molecules, which are in continuous thermal motion. These atomic motions in molecules are well-understood, and follow physical laws similar to those that govern the motions of spring-coupled masses. Vibrational spectroscopy can be observed in both absorption (IR absorption spectroscopy) or in light scattering (Raman spectroscopy) which differ in the way the molecular vibrations are excited and detected; however, both may be described as “fingerprint” techniques, since every molecule exhibits a distinct and specific fingerprint spectrum that allows identification of the molecular compound, and quantitation of its abundance in a sample [13, 14].

For a complex sample, such as human cells or tissues, the observed IR (IR) or Raman spectra are a superposition of all the spectra of the individual biochemical components, and the daunting task of utilizing these techniques for medical diagnosis is to decode the complex spectral signatures. Modern methods of mathematical data analysis, aided by computer algorithms, have succeeded in this decoding process, and the spectral methods are now poised to enter the mainstream diagnostic arena. Preliminary results from a number of laboratories worldwide [15] have indicated that these novel spectral methods can distinguish between normal tissue types, disease types and stages, and even identify the primary tumors from spectral patterns observed in metastatic cells. Furthermore, these techniques can analyze single, unstained and unlabeled cells, and therefore, can be used in the detection of circulating tumor cells [16, 17].

2. Background

The discussion of spectral methods of diagnosis has to start with a short review of the spectroscopies underlying the new methodologies, namely IR (IR) and Raman spectroscopy. In the former, broad-band IR radiation (with wavelength between ca. 2 μm and 20 μm) is focused onto a sample, which absorbs IR radiation at specific wavelength. The light transmitted by the sample lacks these absorbed wavelengths, and thus, presents “absorption spectra” similar to the ones shown in Figure 1. In this figure, several IR absorption spectra are shown for different compounds expected to be found in a cell or tissue. Here, the abscissa is given in “wavenumber” units,

where the wavenumber is defined as the reciprocal of the wavelength, and indicates the number of waves per centimeter. Thus, the units of the wavenumber axis are $1/\text{cm}$ or cm^{-1} . (The reason for choosing this unit is that the wavelength of light is indirectly proportional to the light energy, whereas the wavenumber is directly proportional to energy. Thus, higher wavenumber corresponds to higher photon energy). The ordinate is a logarithmic plot of the amount of light absorbed by a specific vibration, and is presented in “optical density” (OD) units. One OD unit corresponds to 90% of the incident radiation absorbed. Due to instrumental operational parameters, it is not advisable to collect data spectra with more than 1 OD. The spectra reproduced in Figure 1 were “normalized” (see Section 3.3) to account for sample thickness; thus their ordinate values are arbitrary. Furthermore, they were offset along the Y-axis for easier presentation [15].

The spectra shown in Figure 1 can be divided into two regions: the high wavenumber region (2500–4000 cm^{-1} , or 4 μm to 2.5 μm) corresponds to absorptions due to light atom stretching motions: at 3400 cm^{-1} , the O–H stretching vibration is observed, whereas the N–H stretching vibration of the amide backbone is found between 3270 and 3310 cm^{-1} , depending on the hydrogen bonding properties of this proton. C–H stretching vibrations

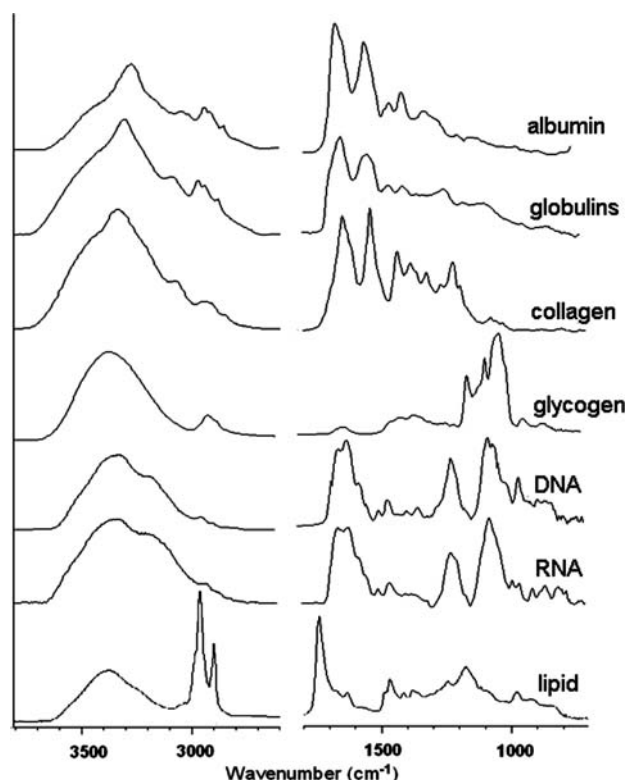


Figure 1 Infrared absorption spectra of selected cellular components.

of aromatic, olefinic and aliphatic C–H bonds occur between ca. 2800 and 3050 cm^{-1} . The 700 to 1800 cm^{-1} region, frequently referred to as the “fingerprint” region, contains in the 1500–1700 cm^{-1} range the vibrations of the protein amide linkage, the “amide I” vibration at ca. 1650 and the “amide II” vibration at ca. 1550 cm^{-1} (see top three traces of Figure 1). For a listing and discussion of many protein vibrational frequencies, the reader is referred to a comprehensive review by Barth [18].

Inspection of Figure 1 reveals that proteins with different secondary structure exhibit quite different IR absorption spectra: helical proteins (such as albumin) exhibit a sharp amide I band at ca. 1655 cm^{-1} , whereas pleated sheet structures exhibit a lower amide I frequency with a distinct high frequency shoulder. This shoulder can be resolved into an individual peak by using 2nd derivative methodology (see Section 3.3). Other biomolecular components of cells and tissues are found in the lower four traces of Figure 1, including polymeric sugars (glycogen) which exhibits strong C–O stretching and C–O–H deformation vibrations between 1000 and 1200 cm^{-1} , DNA and RNA which can be identified by the vibrations of the phosphodiester vibrations (1095 and 1235 cm^{-1}) and aromatic base vibrations between 1600 and 1700 cm^{-1} , and phospholipids with distinct C–H stretching peaks between 2850 and 3000 cm^{-1} in addition to their own phosphodiester vibrations. IR absorption spectroscopy has long been applied to study conformational and other aspects of proteins

and biomolecules [18] and can be considered a mature and well-established field.

The companion technique to IR absorption spectroscopy is Raman spectroscopy [19, 20], which samples the same vibrations that give rise to IR spectra, but using a different excitation mechanism. Instead of illuminating the sample with broad-band IR radiation, the sample is illuminated by intense, monochromatic visible light (typically from a laser). The laser photons are scattered by the molecules of the sample; in the scattering process, the photons lose energy. A plot of the number of photons scattered at given photon energy (wavenumber) yields “Raman spectra” as shown in Figure 2. Again, the abscissa is in wavenumber units (photon energy) and the ordinate indicates the number of scattered photons. Raman and IR spectra are, due to their different excitation mechanism, somewhat complementary and exhibit different sensitivities toward different moieties in the sample. Other differences include the sensitivity of the two methods toward water: IR spectroscopy is strongly confounded by water in the sample, since water is one of the strongest absorbers of IR radiation, whereas Raman spectroscopy is quite insensitive to the presence of water. Raman spectroscopy yields more detail on C–H vibrations, which are particularly strong in this technique. However, Raman spectra are generally weaker, and more difficult to acquire; hence, Raman spectra are generally noisier than IR spectra. IR spectra contain more conformational information on proteins (see Figure 1). Finally, Raman spectra can be collected from significantly smaller spots than IR spectra, and aspect which will be further elaborated in Section 3.2.

When a spectrum of a voxel (pixel) of tissue or a cell is acquired, the spectral information collected depends on the biochemical composition, which varies between tissue types, cell types, location within a cell, state of disease, etc. For example, the cytoplasm of squamous cells may contain glycogen, which manifests itself by a contribution as shown in Figure 1. The nucleus, on the other hand, may show signatures of nucleic acids, in particular during mitosis of a cell. Similarly, structural tissues (such as the stroma, ligaments, cartilage) are rich in collagen, which has a distinct spectral signature. Thus, when IR or Raman spectra are collected from distinct regions or areas of cells or tissue sections, variations in the spectral patterns are observed that can be correlated to the tissue types from which the spectra were collected.

Such spatially resolved spectral data can be collected by carrying out either IR or Raman measurements through a microscope [21]. For Raman microscopy, the instrumentation is very similar to confocal fluorescence microscopy, and utilizes a basic visible microscope to which a laser source and a monochromator for the analysis of the scattered light have been added. The spatial resolution achievable (cf.

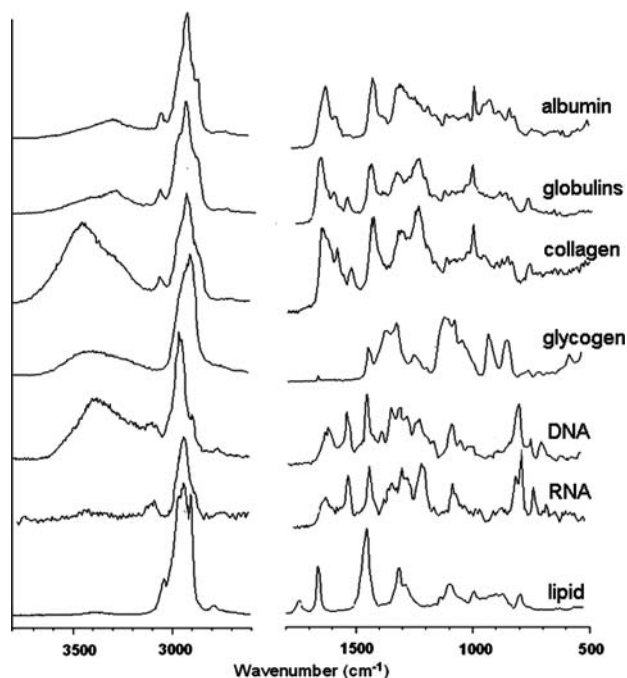


Figure 2 Raman spectra of selected cellular components.

Section 3.2) in Raman microscopy is similar to that of confocal fluorescence microscopy [22].

However, the instrumentation for IR micro-spectroscopy is quite different, since IR radiation is not transmitted by glass. Thus, all optics, including the microscope objectives, are mirror-based. Furthermore, the long wavelength in IR microscopy prevents objects smaller than ca. 10 μm in size to be resolved. Nearly all IR microscopic measurements are performed interferometrically, that is, the signal observed initially is not the desired IR spectrum, but its Fourier transform. Conversion of the interferogram to the spectral domain is carried out automatically *via* the instrument control software.

In the context of this chapter, we shall refer to IR spectroscopy-based medical diagnostics as IR spectral histopathology (IR-SHP). The majority of this chapter deals with this subject. The methodology used in IR-SHP will be elaborated on in more detail in Section 3; may it suffice here to present a very short introduction to this methodology. Unstained tissue sections are used to collect an IR “spectral image”, that is, an image where each tissue pixel is not just represented as a color value (as, for example, in digital photography), but by an entire IR spectrum. Analysis of such a spectral image, to be described in Section 3, yields a pseudo-color rendition of the tissue section that is based on the biochemical composition of the tissue, rather than on the morphology, tissue architecture or staining patterns.

When IR spectral data acquisition is applied to the diagnostics of individual, exfoliated cells, we refer to this technology as IR spectral cytopathology (IR-SCP). IR-SCP can be carried out by collection one spectrum for each cell, or by imaging a cell at a pixel size much smaller than the cell and reconstruction of a cellular spectrum from the individual pixel spectra. This latter approach lends itself to the automatic acquisition of cellular data (see Section 3), and was patented under the name of “PapMap” by some of the authors of this review [23, 24]. The “PapMap” approach has allowed the automatic collection of datasets containing over a million of cellular spectra, and their analysis in terms of origin of the cells, disease state, viral infection, etc.

If Raman spectral data acquisition is applied to tissues, we refer to this method logically as Ra-SHP. Since Raman and IR spectroscopy are complementary techniques, both Ra-SHP and IR-SHP give similar information. However, due to the smaller sampling area in Ra-SHP (see Section 3), the acquisition of Ra-SHP data from large tissue sections is impractical. However, Ra-SHP affords much higher spatial resolution [25, 26] that allows individual cellular components, such as the nucleus [27], or even mitochondria [28] to be detected in the spectral images. Furthermore, it has the enormous advantage of relative immunity from water interference; thus it is

readily amenable to data collection of live tissue or *in-vivo* applications. In fact, several research groups have published numerous reports on Raman histopathology of hollow organs or extracellular matrix [29], or acquired through needles fitted with fiber optics [30–33]. Although the spatial resolution of these methods is less than that of microscopic Ra-SHP, the fact that an entire tissue fingerprint can be collected in a few seconds of data acquisition time bears an enormous advantage for *in-vivo* tissue diagnosis.

Finally, Ra-SCP, the study of individual cells by Raman microscopy will be discussed. Ra-SCP can be carried out in two ways: first, one can utilize the high spatial resolution of the method to collect imaging data sets from one cell, consisting of 10,000 or more individual spectra, and reconstruct a spectral image of this cell. This results in images which can differentiate the individual cellular components such as the membrane, the cytoplasm, the nucleus and nucleoli, membrane-rich structures in the cytoplasm, mitochondria, etc. [34–36]. This method can be viewed as a label-free analog of confocal fluorescence micro-spectroscopy, and can produce images with similarly high spatial resolution. For example, the dynamics, subcellular origin and chemical composition of lipid droplets were monitored in living hepatocytes [37]. However, Ra-SCP imaging does not offer the same contrast that is afforded by antibody-bound fluorophores. Second, Ra-SCP can also be carried out by collecting spectra from individual cells by not utilizing the high spatial resolution (by using longer wavelength excitation and lower numerical aperture objectives) and aiming the exciting laser beam at specific targets in the cell, typically the nucleus. This method is more labor intensive, but yields in relatively short time hundreds of spectra of selected cellular features that show enormous sensitivity toward many biochemical processes, such as the metabolic activity in live yeast cells [38, 39]. For example, this approach has been used very successfully to follow stem cell differentiation [40–42], photochemical changes in melanosomes [43] or for the detection of circulating tumor cells in flow cytometry [16, 17]. Finally, due to the very high spatial resolution of Ra-SCP, spectral information from individual bacterial cells can be collected [44, 45]. This aspect may be of tremendous importance for tracking the origin of bacterial contaminations or outbreaks of infectious diseases, since Raman spectroscopy can, in principle, identify one bacterial particle at the strain level.

3. Methods

This chapter differs from the “Materials and Methods” section in typical research papers in that the

methods used in IR and Raman diagnostic applications are described on a qualitative level without going into the experimental details. In particular, the mathematical steps will be described without equation, but rather, in a pictorial way to introduce the concept.

3.1 Sample preparation

Tissue samples for both Raman and IR data acquisition are prepared as follows. Tissue sections, either from formalin-fixed, paraffin-embedded tissue blocks, or from frozen tissue, are cut *via* a microtome and mounted on suitable substrates. For IR-SHP, the thickness of the sample should not exceed ca. 5 μm if the sample is examined in transfection mode (see below) and not exceed 10 μm for transmission measurements (Figure 3).

For the former case, the substrate of choice is the “low emissivity” (generally referred to as “low-e”) slide that consists of glass with a thin silver coating and an inert overcoat. These slides are completely reflective in the IR spectral region and nearly completely transparent in the visible region; thus, samples on these substrates can be imaged in the IR spectral region, and subsequently stained and imaged with visible light for correlation between classical and spectral histopathology. Unstained tissue sections on the low-e slide are used for IR data acquisition (molecular stains would interfere with data collection); subsequently, they are stained and cover-slipped and used for classical histopathological analysis. Recently, an electric field standing wave artifact has been reported for FTIR microspectroscopy of biological material [46]. As this artifact causes confounding spectral variations related to the sample thickness low-e slide should be used with care. Classical histopathology, along with immunohistochemistry, is used to train algorithms for the automatic diagnosis of IR spectral datasets. For Ra-SHP, tissue sections may be thicker than 10 μm if the Raman data acquisition is carried out confocally, since the thickness of the sampled image slice is determined by the optical arrangement. The substrate for Ra-SHP ideally is a fluorescence free quartz or CaF_2 slide, although we have recently collected good Ra-

SHP datasets from 5 μm thick tissue sections mounted on low-e slides as well [47].

After mounting tissue sections on appropriate substrates, the samples are air dried, which can be considered an effective way of fixation because the samples are resistant toward further degradation and remain virtually unaffected for days or weeks [48, 49]. On the other hand, dehydration causes denaturation of biomolecules such as lipids, proteins and nucleic acids. Hydrophobic lipids such as cholesterol and cholesterol ester form microcrystals, proteins precipitate and become insoluble, and DNA changes conformation from the normal B-form towards A- or unordered forms [50]. This denaturation can be prevented by keeping the samples moist or transferring them into aqueous buffer during data acquisition. Whereas it is more challenging to collect IR data from such samples due to the strong mid-IR absorbance of water, Raman data can easily be collected and enable to transfer the results to *in vivo* conditions.

For IR-SCP, we have found that spin-depositing cells from a suspension, using a cyto-centrifuge, onto a low-e slide works very well. Depending on the concentration of cells in the original suspension and the deposition time, sparse monolayers of (unstained) cells can be produced. For relatively large squamous epithelial cells, we typically aim for about 50 cells/ mm^2 . Cells generally adhere well to the low-e slides, which may be coated by poly-L-lysine to improve adhesion. This method lends itself to the automatic collection of SCP datasets. Cultured cells can be grown directly onto IR-compatible substrates. Cells may be stained after IR image acquisition for classical cytopathological analysis.

For Ra-SCP, few μL of a cell suspension typically are dropped onto a quartz or CaF_2 slide and allowed to dry. Cells are selected under a microscope for data acquisition. This mode of data acquisition lends itself to the analysis of large numbers of cells, and has been used widely [40–42, 51]. However, in the context of this chapter, another imaging based method for Ra-SCP data acquisition will be introduced. Since we were interested studying to the uptake and distribution of drugs into cells, we have allowed cells to attach themselves to a substrate before they are treated, *in vivo*, with drugs or drug delivery systems. After incubation times that vary between a few min-

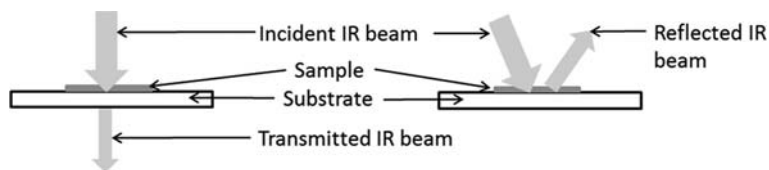


Figure 3 Measurement in infrared transmission (left) and transfection (right) mode. In transfection mode, the IR beam passes through the sample, is reflected by the Ag layer covering the substrate, and passes the sample again, before reaching the detector.

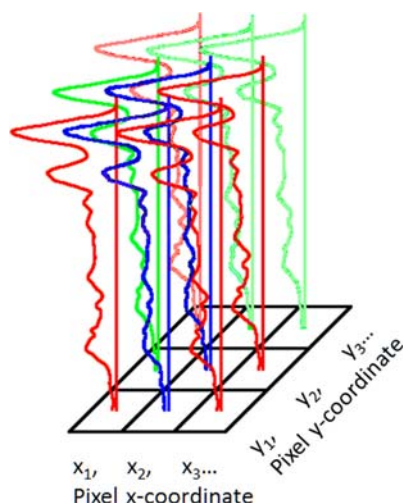


Figure 4 Schematic diagram of a hyperspectral data cube.

utes to 24 hrs, cells were fixed, and imaging datasets were collected, using a water immersion objective, of cells in their native aqueous surrounding. The use of imaging methods (see next section) allows exact locations of drug and drug carriers to be determined.

Non-adherent cells such as blood cells or cells in other body fluids (saliva, urine, cerebrospinal fluid) can be studied by Raman spectroscopy with minimal sample preparation. If the Raman excitation laser is focused onto the cell, the high electric field acts as laser tweezers retaining the cell inside the focus during data acquisition. Optical traps are formed by two counter-propagating lasers that enable separation of Raman excitation and micromanipulation of cells. These optical tools are compatible with microfluidic devices and pave the way towards Raman activated cell sorting: cells are injected into microfluidic channels, optically trapped, identified by their Raman spectroscopic signature and subsequently sorted.

3.2 Collection of hyperspectral data cubes

IR and Raman imaging methods contain both spatial and compositional information in one measurement, similar to immunohistochemical imaging technology. However, as pointed out above, Raman and IR data are collected from inherent spectral fingerprint signatures, and do not require any external dyes or labels. In IR-SCP and IR-SHP, spectra are collected from voxels of tissue about $10\ \mu\text{m} \times 10\ \mu\text{m}$ in the lateral (x, y) dimensions and about $5\ \mu\text{m}$ in the axial (z) direction. The latter is determined by the thickness of the tissue or cell, whereas the lateral dimensions are determined by a physical quantity known as the diffraction limit, which depends on the wavelength of light, and the numeric aperture (NA) of the micro-

scope objective. In RA-SHP and RA-SCP, the wavelength of light is much smaller than in the corresponding IR methods; consequently, smaller voxels can be illuminated: for high resolution work from the LSpD to be described later, lateral dimensions were ca. $300\ \text{nm} \times 300\ \text{nm}$, with an axial resolution of ca. $1\ \mu\text{m}$. For the RA-SCP studies reported by other groups, the lateral dimensions often exceed $1\ \mu\text{m} \times 1\ \mu\text{m}$ [27].

In both Raman and IR-based imaging methods, spectra from sampled pixels are collected and arranged as “spectral hypercubes” or “hyperspectral data cubes”, shown in Figure 4. The bottom of this graph shows the pixels (or voxels) from which spectral data were collected along with voxel coordinates; the spectra themselves are indicated by the vertical wavelength (or wavenumber) axis, and the spectral intensities as shown. Further dimensions can be introduced, such as the axial coordinate in confocal microscopy, or the time domain for time dependent experiments. Such a spectral hypercube contains all the pertinent information of the tissue composition and its spatial variations; however, in its raw form, it is useless for medical diagnostics. Thus, data processing is carried out on this hypercube to present the spectral information in a suitable form for medical diagnosis. Each spectrum in the data cube is stored as a “spectral vector”, which typically contains a column of wavenumber values, each followed by intensity (Raman scattered intensity or IR absorption) values. If the data points in a spectral vector are equidistantly spaced, it is sufficient to store an initial wavenumber, the number of points and an increment value to save storage space.

The size of a hyperspectral data cube depends of course on the size of the tissue or cell to be imaged. Tissue sections often measure several square millimeters in size. Given the pixel (voxel) dimensions discussed above, a $3\ \text{mm} \times 3\ \text{mm}$ tissue section would produce a hyperspectral dataset consisting of $300 \times 300 (= 90,000)$ spectra. Since each spectrum typically consists of about 1500 intensity/wavelength data points, such a dataset easily occupies around a GByte of disk space. Due to the much smaller pixel size in Raman imaging, a 100×100 pixel dataset will typically only cover an area of $100\ \mu\text{m} \times 100\ \mu\text{m}$ to about $1\ \text{mm} \times 1\ \text{mm}$.

3.3 Data pre-processing

A number of recent publications [23, 52, 53] have dealt with data pre-processing steps and methods, particularly for IR-based measurements, which will not be detailed here. These steps are necessary since any experimental data are contaminated by noise, unwanted spectral features, distortions etc., the source

of which are well-understood. Most important are corrections for Mie-scattering contributions that can shift observed peaks and cause intensity distortions [54, 55]. Furthermore, data sometimes are collected in domains that are not suitable for further data analysis (time *vs.* frequency domains, for example) and need to be converted from one into the other by a procedure known as Fourier transformation (FT). All magnetic resonance imaging (MRI) data, for example, are recorded in the time domain and converted, *via* FT, to the frequency domain. Similarly, raw IR spectra are produced by FT from interferometrically acquired data; hence, IR methodologies are often referred to as FTIR spectroscopy.

IR spectra may be superimposed on sloping baselines that confound computer interpretation of spectral features. Thus, spectral interpretation is frequently carried out on 2nd derivative spectra; the process of calculating the second derivative of the intensity with respect to the wavenumber removes baseline fluctuations and reduces the apparent width of the spectral peaks. The intensity of IR spectra depends directly on the path the IR beam travels through the sample; consequently, the sample thickness determines the observed absorption strength. To account for variations in sample thickness of a cell or tissue section, the second derivative spectra are normalized.

Raman spectral data need to be corrected for spectral spikes that result from the interaction of cosmic rays and the detector elements, and should be converted to linear wavenumber scales. As Raman data are generally too noisy to warrant conversion to 2nd derivatives a baseline is subtracted from the spectra to correct for auto-fluorescence background. Although it has been noted that the auto-fluorescence can contribute to the distinction of tissue types (e.g. normal versus non-normal), it usually exhibits too low specificity for accurate differential diagnosis. Then, the spectra are normalized to compensate confounding variations in sample thickness, laser focus and penetration depth.

The pre-processing procedures listed above generally are applied consecutively to each spectrum in a dataset; given the size of the hyperspectral datasets (see Section 3.2), preprocessing amounts to a substantial computational effort that may take a few minutes computation time.

3.4 Pre-sorting (cluster analysis)

The goal of spectral diagnostic methodology is the recognition of tissue spectral features, and to utilize these features to aid in medical diagnoses. As pointed out above, the raw data contained in a spectral hypercube cannot, *a priori*, be used for this purpose, and methods need to be developed to accomplish this

task. Most of the researchers in the field of optical diagnosis *via* vibrational spectroscopy have adopted a diagnostic scheme that is summarized in Figure 5. The data-processing step starts with the pre-processed hyperspectral (Raman or IR) dataset of the unstained tissue, and converts it into a pseudo-color image. This step, in principle, could be performed by color coding an intensity value (e.g., red: high, blue: low) at a given wavelength, and plotting the color codes at the pixel coordinates. Similarly, intensity ratios, band positions (wavenumbers) or half-width could be encoded as well. However, these so-called univariate methods (because only one intensity value of a spectrum is used) are counterproductive in the sense that the rest of the information contained in the spectra is not utilized. Multivariate methods, in contrast, utilize the entire spectral vectors to create images from the hyperspectral datasets. One commonly used multivariate method is unsupervised hierarchical cluster analysis (HCA) [21, 56] which calculates the similarity of all spectra in a dataset, and assigns color codes to spectral groups, or clusters, based on their similarity. Figure 5 shows such an HCA-based spectral image and, for comparison, an H&E-stained image of the same tissue section (see Section 3.5). It should be emphasized at this point that the conversion of the hyperspectral data cube into the HCA image is completely “unsupervised”, which in this context implies that the HCA algorithm needs no training, but arrives at the pseudo-color HCA image strictly by a mathematical comparison of spectral similarity.

3.5 Visual imaging

At this point in the diagnostic procedure, the tissue section is stained (typically using H&E stain) and imaged, using a visual microscope at 20× or 40× magnification and a high resolution digital camera. A comparison between the H&E digital image and the HCA image, based on the IR or Raman datasets, shows a very high correlation between the tissue boundaries apparent in the H&E image, and the boundaries in the HCA image (see Figure 5). This indicates that IR spectra detect changes in tissue composition that parallel the different pathological features observed in the H&E image. The images generally are aligned with respect to each other using prominent tissue features.

3.6 Annotation

The next step toward training a diagnostic algorithm to automatically detect and assign tissue types or dis-

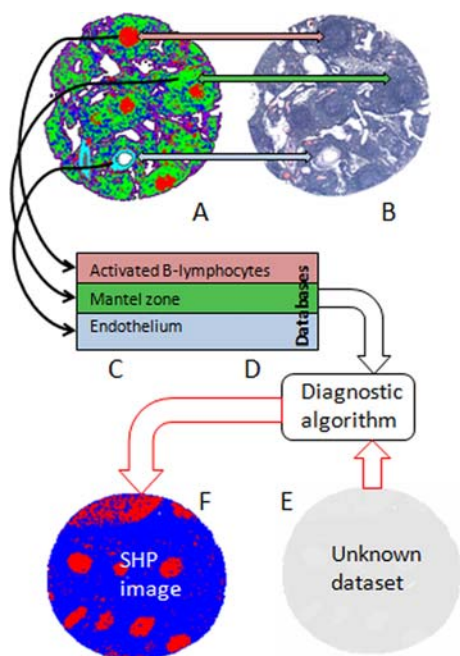


Figure 5 Schematic of SHP Process. (A) Pseudo-color image of tissue section obtained from hyperspectral data cube by HCA. (B) Photomicrograph of same tissue section, H&E stained after IR data acquisition. (C) Data bases extracted from HCA image during annotation process. (D) Diagnostic algorithm trained with database “C”. (E) Hyperspectral dataset from unknown sample. (F) Pseudo-color SHP image produced by diagnostic algorithm to distinguish activated B-lymphocytes from other tissue types.

eased areas is the correlation of spectral regions identified by the HCA map with regions that can be recognized by a pathologist in the H&E images. To this end, corresponding regions in the HCA image and the H&E image are selected, as indicated by the black arrows in Figure 5. Spectra from the selected areas are extracted and tagged with a diagnostic code, for example, activated B-lymphocytes (red areas in Figure 5), or endothelial cells (light blue areas). The selected spectra are entered into a database for subsequent training of diagnostic algorithms. This annotation step is necessary only during the training phase of a diagnostic algorithm or to es-

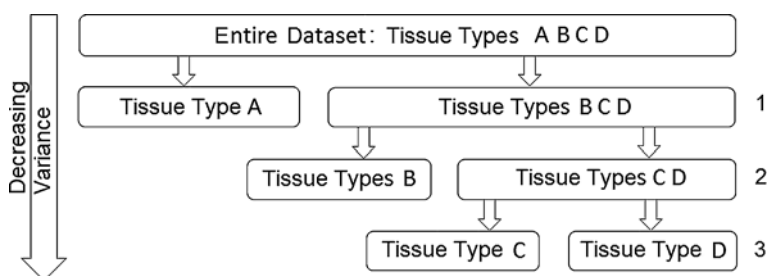
tablish an annotated database for algorithm testing; however, this step is omitted for the diagnostic analysis of an unknown sample.

3.7 Diagnostic data analysis

As indicated earlier, the overall goal of the optical diagnostic methods is to provide medical information on a tissue section that is based on chemical composition and compositional variations, rather than on morphological criteria. In order to correlate the compositional changes with disease, self-learning mathematical algorithms are utilized that correlate spectral (compositional) changes with any other available diagnostic information, such as immunohistochemical or – particularly in the early stages of development – classical staining and morphological changes, disease outcome, etc. Thus, the self-learning algorithms for analyzing spectral data may be based on morphological correlations, although the goal of these efforts is to move away from the morphological descriptors, and utilize strictly compositional aspects of the tissue samples.

After establishing databases of annotated spectra from many patients with the same disease diagnosis, algorithms are trained to recognize the distinct spectral features associated with a particular disease. Although it is possible to train self-learning algorithms that recognize several disease states and tissue types, it is advantageous to design an algorithm tree, or a set of hierarchical algorithms that analyze the data in consecutive binary steps, as indicated in Figure 6. Depending on the tissue type and disease state, it may be advantageous to distinguish the most different class of spectra first. In breast cancer, for example, the most different tissue type may be adipose tissue, whereas in certain blood cancers, it may be advantageous to test for the spectral class of erythrocytes first. Subsequently, spectral classes with the next highest variance may be differentiated, for example molecular subtypes of breast cancer [57]. Thus, the diagnostic algorithm may be broken down into a set of binary decision steps. The order of the binary decision steps may be determined by classical

Figure 6 Schematic of a hierarchical decision tree for tissue diagnostics. Each of the endpoints (pure Tissue type A, pure Tissue type B, etc.) could be the starting point for further algorithms for a finer discrimination (tissue subtypes).



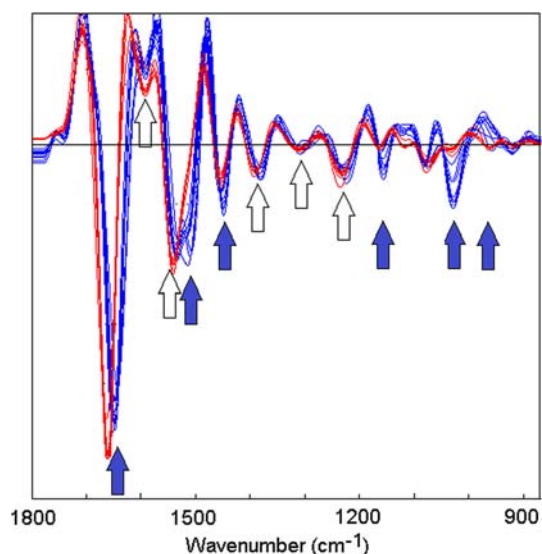


Figure 7 Feature selection to discriminate two spectral classes (red and blue), with relevant features given by blue arrows.

methods of multivariate analysis *via* spectral covariance, or by performing hierarchical clustering of the spectra in the annotated database.

The training of each of the binary decisions consists of the following steps, explained here for the case of a binary decision between two spectral classes, A and BCD (see Figure 6). First, a “feature selection” is being carried out that utilizes hundreds or thousands of spectra in each of the databases of classes A and BCD to determine which spectral intensities, or “features”, can reliably differentiate between the two classes. Although the feature selection is a mathematical process, a pictorial view of this process is presented in Figure 7. Here, a set of spectra from two classes is shown, along with spectral features, indicated by blue arrows that allow discrimination of the two classes. Note that other peaks, indicated by the white arrows, do not contribute to the discrimination, since the spectral differences are either weak or not unique. Thus, feature selection can be viewed as a process that removes irrelevant features from the data. A typical fingerprint region spectral vector may consist of about 500 intensity points; typically about 1/10 of those are useful in discriminating the spectral classes. Several mathematical methods exist, for example, as MATLAB library functions (The Mathworks, Natick, MA, USA) to carry out feature selection.

Next, a self-learning algorithm is trained to quantitatively discriminate between the spectral classes A and BCD. Recent progress in chemometric methods [58] has led to several algorithm types based on artificial neural networks (ANNs), support vector machines (SVMs), random forests (RFs) and others. Their performance, when properly trained and vali-

dated, is quite similar, and we shall use ANNs for an example for the following discussion. For unbiased training and test runs of the ANN, the dataset is split into completely independent training and test sets. A typical number of training spectra in applications reported by us would consist of 6000 spectra, from 12 patients, for tissue class A, and 6000 spectra of classes BCD, equally divided between classes B, C and D (2,000 spectra each, from 4 patients in each class). The ANN in the training phase “learns” to associate the selected spectral features with the diagnostic outcome; in particular, it assigns “weights” to each of the features to achieve an optimal balance between the sensitivity (which evaluates the percentage of true positive diagnoses) and the specificity (which evaluates the percentage of false negative diagnoses) against a gold standard. For the training set, the outcome (sensitivity and specificity) is generally very high, >98%. When applying such a trained algorithm to the test data set, the sensitivity and specificity typically are better than 80%, often even better than 90%, if sufficiently large datasets are utilized, and if the annotation (step 3.5 above) is carried out sufficiently carefully by a pathologist to give pure class spectral databases.

3.8 Visual data analysis: factor methods

Several factor methods have been developed for SCP and SHP to decompose data sets into a bilinear model of variables. Similar to HCA discussed above, factor methods are unsupervised and can reveal small, but recurring spectral differences in a dataset. Because different mathematical solutions exist for decompositions, further constraints are introduced. In principal component analysis (PCA) [58], a set of new spectra, known as principal components (PC) or loading vectors is calculated from the covariance matrix of the entire dataset. These PCs contain, in order of decreasing magnitude, the variance in the dataset: the first PC might, for example, be the mean (average) of all spectra, the second PC the largest deviation from the mean, and so on. Usually, only about 30 PCs are needed to capture nearly all (99.5%) the variance in the dataset, which implies that the original dataset can be expressed as linear combinations (mixing) of these thirty or so PCs. Furthermore, it is assumed that similar spectra in the original dataset require the same PCs, and the same abundances of these PCs, to reconstruct the spectra. When plotting the contributions (scores) of one PC vs. the contributions of another PC, a ‘scores plot’ is obtained that can show whether spectra are related to each other, or not.

Vertex component analysis [59] and N-FINDR [60] are other factor methods that have recently

been introduced. They decompose a hyperspectral dataset into linear combinations of endmember spectra which are considered the pure “component” spectra. The VCA algorithm, for example, finds the most different spectra in a dataset of spectra and considers them to be the endmembers. Subsequently all spectra in the dataset are reconstructed in terms of these endmembers. This is similar to the decomposition of a spectral dataset into its principal components except that in VCA the most dissimilar spectra are used as endmembers, whereas in PCA the spectra containing the most variance are used as basis for the decomposition. One constraint in VCA is that the concentrations, or abundances, of the endmembers are non-negative. Further details have been given elsewhere [61, 62].

4. Results and discussion

Our foray into SHP and SCP started, similar to the early steps taken by several other research groups, with attempts to detect and differentiate different stages of cervical disease, both in exfoliated cells as well as cervical biopsies. In the former case, we quickly realized that the problem was untraceable in the late 1990's and early 2000 due to the lack of understanding of many of the spectral problems associated with single cell spectroscopy (see Section 4.3.1), and the need to collect ten thousand to hundred thousand cell spectra to arrive at statistically significant results. For cervical tissue samples, the heterogeneity of normal tissue, with enormous variations in glycogen concentration in the squamous epithelium, and sometimes ill-defined diagnoses in the cases of mild cervical disease, presented serious problems in the original work. Thus, we decided on a problem that seemed better defined in terms of diagnosable disease, namely the detection of metastatic cancer cells in lymph nodes tissue. Indeed, this problem proved to be quite amenable to study via IR-SHP, and yielded interesting insights into the immune response of the body toward cancer cells.

4.1 IR-SHP: Detection of metastases and micro-metastases in lymph nodes

The earliest results were obtained for lymph nodes with large metastatic cancer regions, which were easily visible in stained tissue, and which had a readily accessible medical diagnosis. One of the earliest results obtained is shown in Figure 8, which depicts a section from an excised lymph node with a well-defined region of metastatic colon adenocarcinoma.

The images were obtained using a pixel size of $25\ \mu\text{m} \times 25\ \mu\text{m}$ (larger than what is presently used) and unsupervised cluster analysis (see Section 3.4) to construct the pseudo-color images. Thus, the images shown in Figure 8 are not based on any diagnostic input, but strictly use the spectral information in the IR-SHP dataset to distinguish tissue types.

Panels A and B of Figure 8 depict an H&E-stained photomicrograph of an entire lymph node section, measuring about $8\ \text{mm} \times 8\ \text{mm}$ in size, and the corresponding IR-SHP pseudo-color image obtained by HCA, respectively. In Panel B, the tumor (dark red) is differentiated well from the medullary sinus (light blue), the germinal centers (red), the T-lymphocytes (dark blue) and the capsule (yellow and blue-gray). Here, there is no pathological ambiguity in the diagnoses of cancer and normal tissue, and the IR-SHP results very well agree with the visual image. Panels C and D present enlarged sections of the same lymph node, containing only normal tissue. In Panel D, the germinal centers (dark brown), surrounded by the mantle zone (dark blue) are clearly visible, indicating, for the first time, the spectral differentiation of B-lymphocyte activation: the germinal centers in a lymph node are activated by an antigen, here most likely originating from the cancer in the adjacent tissue. This B-lymphocyte activation is accompanied by high proliferation rates, which change the chemical composition observable in IR-SHP. In Panel D, the capsule of the lymph node (orange region) is also recognizable; this region consists of fibro-connective tissue which has a significantly different chemical composition which is easily recognized in IR-SHP. These results demonstrated the enormous sensitivity of IR-SHP, because the biochemical differences between activated and non-activated B-lymphocytes are quite subtle, yet are recognized by spectral methods. These results also demonstrated unambiguously that a region of adenocarcinoma has biochemical characteristics which are significantly different from those of B- and T-lymphocytes and normal structures in lymph nodes.

Figure 8 also demonstrates one limitation that was discovered early during this work. The cluster analyses shown in Panels B and D were carried out omitting the amide I spectral range, since the bands in this region were contaminated by spectral artifacts due to Mie-scattering of the lymphocytes. Mie-scattering is a well-known effect in classical physics and occurs when the light incident on spherical sample particles has about the same wavelength as the size of the particles (see Section 3.3). In addition to producing broad, undulating background features superimposed on the absorption spectra of the sample, Mie scattering also can mix the reflective and absorptive components of the interaction of radiation with the sample; this mixing, which has been referred to as resonance-Mie (RMie) scattering [55,

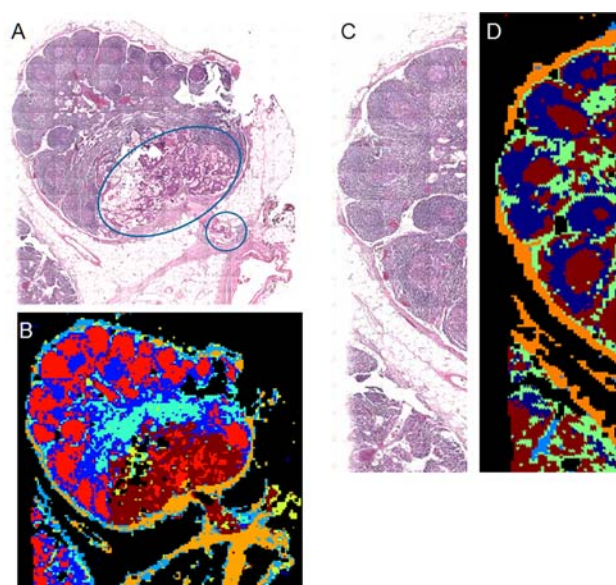


Figure 8 (A) Photomicrograph of an 8 mm \times 8 mm lymph node tissue section with a colon cancer metastases (in blue ellipse and circle). (B) HCA-based pseudo-color image of section shown in (A) depicting different tissue types, including the adenocarcinoma (dark red). (C) Photomicrograph of partial section of same lymph node, showing reactive lymph node follicles. (D) HCA-based pseudo-color image of the section shown in (C); demonstrating the distinction between activated (dark brown) and non-activated (dark blue) B-lymphocytes (dark blue) by IR-SHP.

63, 64] can cause severe distortion of the absorptive line shapes observed in IR spectroscopy. This distortion causes an apparent shift in the band position (up to 40 cm^{-1} in extreme cases), and severe distortions of observed intensities. The interference between absorption and scattering effects has been the subject of several recent papers [64, 65], and several approaches have been developed to account for them [55, 65, 66]. In more recent spectral images reported later in this review, these artifacts have been accounted for in the pre-processing methods described in Section 3.3.

4.1.1 IR-SHP of micro-metastases in lymph nodes

Although the detection and diagnosis of large metastases, such as the one shown in Figure 8, in lymph nodes does not present any difficulty for a pathologist, the detection of very early and consequently very small metastases by classical histopathology often is difficult. Metastases in a lymph node are

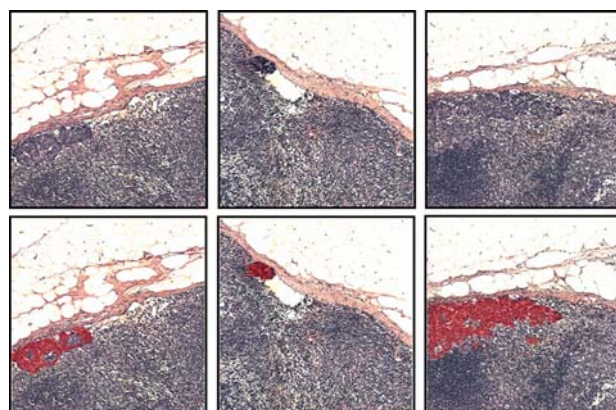


Figure 9 Top row: photomicrographs of H&E stained, 1 mm \times 1 mm section of auxiliary lymph nodes harboring micro-metastases. Bottom row: overlay of HCA-derived regions indicating tissue abnormalities.

formed when cancer cells break loose from the primary tumor site and travel as ‘circulating tumor cells’ through the blood and lymph system. In the latter case, they may be filtered out in the lymph nodes and start metastases, mostly in the medullary sinuses. In the earliest stages, these metastatic sites can be considered single tumor cells which subsequently may divide rapidly to form metastases. By definition, a metastasis less than 2 mm in size is considered a micro-metastasis, although in this stage, they already may contain hundreds of thousands of cancer cells. Images of a lymph node section with a micro-metastasis are shown in Figure 9.

The detection of micro-metastases or small clusters of cancerous cells in lymph nodes *via* standard histopathology is a formidable task owing to the small size and lack of distinguishing features of the abnormality within the lymph node tissue. Yet, the detection of these micro-metastases is of prime importance to stage the spread of disease: if a lymph node is found to be free of metastatic cells, it is thought that the spread of cancer has been contained. On the other hand, a false negative diagnosis, i.e., a missed micro-metastasis in a lymph node, presents too optimistic a diagnosis, and a more aggressive treatment should have been indicated.

The primary method for the detection of micro-metastases to date has been standard histopathology. Excised lymph node tissue, typically from the sentinel lymph node (the lymph node closest to the tumor), are sectioned, stained and analyzed by visual inspection under a microscope. If micro-metastases are suspected, immunohistochemical agents/counter stains such as cytokeratin specific stains [67] may be used to enhance the sensitivity of classical histopathology. However, this procedure is time consuming and costly, and still relies on the human eye for detection. The problem is further complicated in that

many sections need to be diagnosed since the volume of a micro-metastasis is small compared to the volume of a lymph node, and could easily be missed if just one section of a lymph node was analyzed. Consequently, we started an investigation that involved collecting 50 IR spectral datasets, each from a 1 mm × 1 mm area of lymph node tissue adjacent to the capsule [68–70]. Each lymph node in this study was excised during cancer surgery, and was known to harbor micro-metastases. However, not all sections actually contained micro-metastases, since the sectioning process easily may have missed a small cancerous region.

When this study was undertaken, the correction of scattering effects in tissue IR spectra had not succeeded; consequently, the cancerous regions from different lymph nodes could not easily be compared, and supervised algorithmic analysis of the cancer spectra from different lymph node sections was impractical. However, within a given lymph node section, the distinction of cancerous regions from the capsule and the (activated or non-activated) lymphocytes with the lymph node proved to be reliable and practical, see Figure 9. SHP detected micro-metastases in 5 of the total of 50 tissue sections, and all metastatic regions were confirmed by visual pathology. In addition, a micro-metastasis was found in a section that was originally missed by classical histopathology, but later confirmed by this method. These results pointed to the feasibility of using spectral methods for routine pathological tasks, and to the fact that the sensitivity of an instrument and computer-based method can be higher than that of classical methodology.

Most interestingly, in the lower right panel in Figure 9, individual metastatic cancer cells were detected by SHP, and one instance of phagocytic histiocytes attacking metastatic cancer cells. In fact, the spectra of these histiocytes clustered with those of the metastatic cells, indicating that the molecular components of the cancer cells were still detectable by SHP, although the cancer cell had effectively been destroyed [68].

4.1.2 IR-SHP of lymphocyte activation in lymph nodes

This section describes very recent results from a study that is aimed at establishing that SHP can differentiate the activation process of B-lymphocytes in lymph node tissue. This study follows several other references in the literature that have established that spectral diagnostic methods can

- identify the sites of primary tumors in metastatic cancers in the brain [71],

- differentiate metastatic cancers from different primary tumors in lymph nodes
- differentiate between different tumors in the same organ [72]
- detect spectral changes due to overexpression of individual cancer markers [73].

Thus, we wanted to establish whether SHP is able to differentiate the activation of lymphocytes in lymph nodes due to different primary cancers. Here, the paradigm of the studies is as follows: the activation of lymphocytes is initiated when antigen-presenting cells expose lymphocytes with specific molecular signatures of disease; in this case, specific or nonspecific binding of the antigen to B-cell antigen receptors occurs [74]. This binding initiates a cascade of events involving B-cell antigen receptor (BCR) molecules, which are immunoglobulin proteins found at the cell membrane. These events eventually lead to the production and activation of many other immune cells, such as histiocytes and macrophages, which can specifically attack and destroy cancer cells. Since different cancers exhibit different spectral patterns in SHP, and since cancer metastases can be differentiated by SHP, we hypothesized that lymphocyte activation by different cancers may be distinguished as well by SHP.

To this end, a tissue microarray (BiomaxUS, LN802) was used that contained biopsies from sentinel lymph nodes of both adenocarcinomas (ADC) and squamous cell carcinomas (SqCC) of the stomach, esophagus and the colon. The majority of the tissue cores utilized for this project maintained well-defined tissue architecture, as illustrated in Figure 10. Both the H&E stained photomicrograph and HCA pseudo-color map images agree on the location of the germinal centers (HCA dark green clusters) surrounded by the mantle zone (cyan clusters) comprised of non-activated B-lymphocytes surrounding the germinal centers (activated B-lymphocytes).

The following discussion only includes lymph nodes from patients diagnosed with some form of cancer. These nodes were resected during surgery

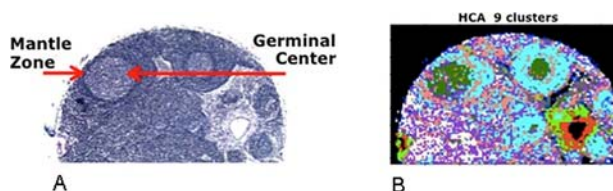


Figure 10 (A) Photomicrograph of an H&E – stained lymph node tissue section on a tissue microarray showing several germinal centers and the mantle zones surrounding them (B) HCA pseudo-color image demonstrating the spectral distinction of germinal centers (dark green), mantle zone (light blue), endothelial cells (orange) and the remainder of the lymph node tissue.

for the primary cancer – of colon, stomach, or esophagus, but were free of metastatic cancer cells. However, they all showed distinct germinal centers due to B-lymphocyte activation. In order to evaluate the changes due to B-lymphocyte activation, only lymph node cores with clear and distinct germinal centers identified by a pathologist were used for analysis. These cores are shown in Figure 11, where photomicrographs of the H & E stained cores are on the left and a corresponding binary HCA pseudo-color map on the right. These HCA images are color-coded to display germinal centers in red and all remaining tissue types in blue. Several hundred individual spectra were extracted from multiple germinal centers of each lymph node section and placed into databases for later processing. These spectra represent B-lymphocytes activated by the presence of a malignancy in the body, and were subsequently scrutinized by Principal Component Analysis (PCA, see Section 3.8) to determine if SHP can differentiate the different cancer types leading to lymphocyte activation. Results from these efforts are shown in Figure 12.

This Figure displays a PCA scores plot of the extracted B-lymphocyte pixel spectra from lymph nodes activated by primary cancers of the stomach, esophagus, or colon, and demonstrates that differences in activation of B-lymphocytes originating from different adenocarcinomas can be detected by SHP. The spectral class of colon ADC is comprised of equal number of spectra from two patients, whereas the matched number of spectra of ADC of esophagus and stomach are from one patient each. In a prior study, we have shown that patient-to-patient spectral variations generally are smaller than those produced by disease [47]. Also shown in Figure 12 are the PCA loading vectors PC1 and PC2 along which the spectra are separated. In this plot, loading vector 2 (Figure 12c) is mostly responsible for the separation between the three classes. Here the largest changes are observed in the amide I, ca. 1655 cm^{-1} , phospholipid, ca. 1164 cm^{-1} , and DNA, ca. 1090 cm^{-1} , regions. Loading vector 1 (Figure 12b) separates the spectra representing ADC of the stomach from ADC of colon and esophagus. The main bands distinguishing loading vector 1 are located at typical DNA frequencies at 1090 cm^{-1} and 1250 cm^{-1} with significant changes in the protein region as well. The spectra extracted from the germinal centers were normalized separately in two regions, $1800\text{ to }1380\text{ cm}^{-1}$, and $1378\text{ to }776\text{ cm}^{-1}$, with the demarcation between the two normalization regions shown by the red arrow in Figures 12b and c. Separate normalization (commonly employed in bacterial identification by spectral methods [75]) of the protein and DNA/RNA/lipid spectral regions better represents the abundances of these components in cells and tissues.

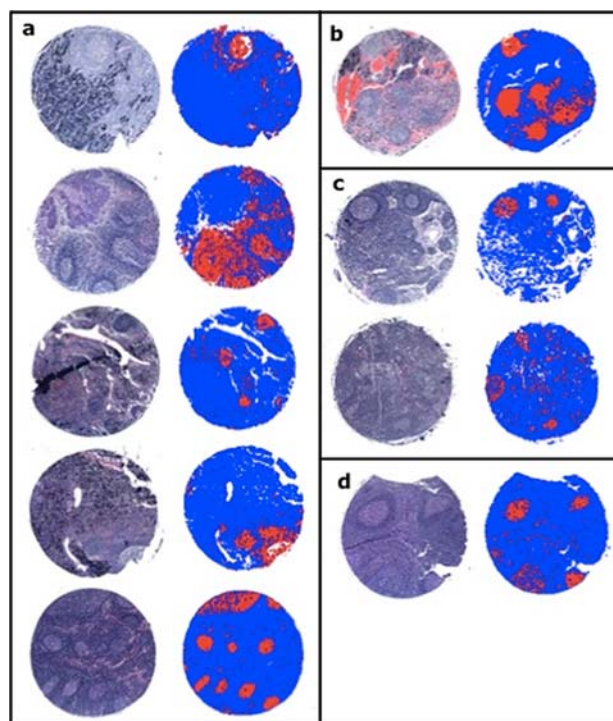


Figure 11 Representative tissue spots included in the analyses presented. Photomicrographs of H & E stained cores (left) with their representative binary pseudo-color maps (right) where activated B-lymphocytes (germinal centers) are shown in red and non-activated tissue in blue. (a) SqCC of esophagus, (b) ADC of esophagus, (c) ADC of colon, (d) ADC of stomach.

While the IR spectra of germinal centers suggest the possibility of identifying the type of tumor cells a sentinel lymph node is exposed to and provides information on global changes occurring in the lymph node, Raman SHP affords a more detailed investigation of the molecular changes associated with B-lymphocyte activation. To this end, Raman micro-spectral images were acquired from a small area of a germinal center and the surrounding mantle cell region; such a map is shown in Figure 13. Panel A depicts the activated lymphocytes in the germinal center (upper left) and the dense layer of lymphocytes in the mantle zone, extending in an arc from the lower left to the upper right corner. The area imaged by Raman SHP is shown by the red square in Panel A, and is shown magnified in Panel B. Panel B was reconstructed from the Raman dataset by an algorithm known as Vertex Component Analysis (VCA) which was discussed in Section 3.8.

Subsequently, images are constructed by overlaying the abundance images for each endmember. The purple/blue areas of Panel B correspond to endmember (a) in Figure 13C. This endmember describes the average composition of the lymphocytes in both the germinal center and the mantle zone.

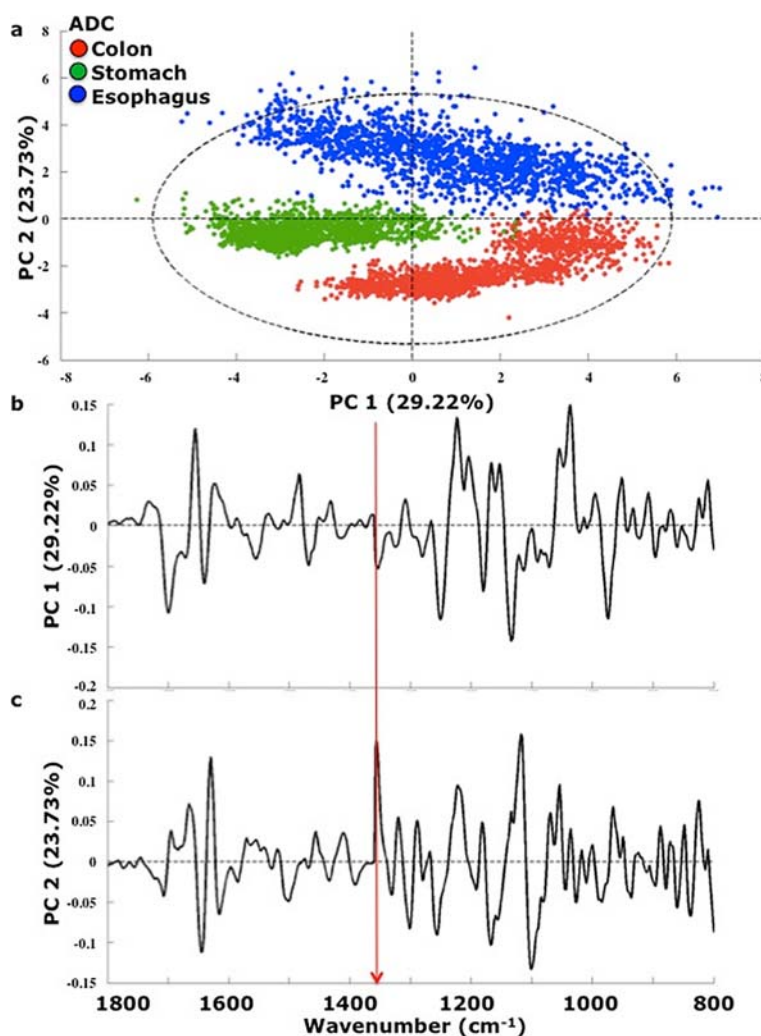


Figure 12 PCA scores plot of activated B-lymphocytes originating from lymph nodes resected near the stomach (red, 1 patient), colon (green, 4 patients), and esophagus (blue, 5 patient). These normal lymphocytes are activated due to the presence of a carcinoma in the designated organ: stomach adenocarcinoma, colon adenocarcinoma, and esophageal squamous cell carcinoma, which are the most prominent for humans in these organs.

The yellow dots in Figure 13B denote the nuclei of cells in the mantle zone; these nuclei contain another distinct biochemical compound that distinguishes them from the nuclei of activated cells in the germinal center. The endmember spectrum corresponding to the nuclei in the mantle zone is shown in trace (b) in Panel C. An image similar to Panel 13B was also obtained by HCA.

It is interesting to note that the difference between activated and non-activated lymphocytes is reduced by VCA to one major spectral component (trace b in Figure 13C). cursory inspection of this spectrum points to a phospholipid, and a more detailed search points to phosphatidyl-choline (see trace c in Figure 13C) or similar phospholipids, as the cause of the spectral differentiation. Thus, the spectral difference between activated and non-activated B-lymphocytes is due to a change in phospholipid contributions. This result is confirmed by previous literature, which reported the breakdown of phospholipids, such as phosphatidyl-inositol, when B-lymphocytes were activated *in vitro* [76].

4.2 SHP of squamous cell carcinoma and adenocarcinomas

4.2.1 Distinction of different cancer types by IR-SHP

In this section, we shall present results that demonstrate that SHP can reliably differentiate different cancers occurring in the same organ. Most SHP studies to date, by us and others, have concentrated on differentiating different normal tissue types from cancerous tissue and inflammatory response. The only exceptions to this were the early efforts to identify the primary tumors causing cancer metastasis in the brain [71], in which spectral methods clearly could distinguish different cancer types and primary sites.

Here, we wish to summarize efforts that have spanned the past 18 months to differentiate different cancer types, as well as their grade, by SHP. This

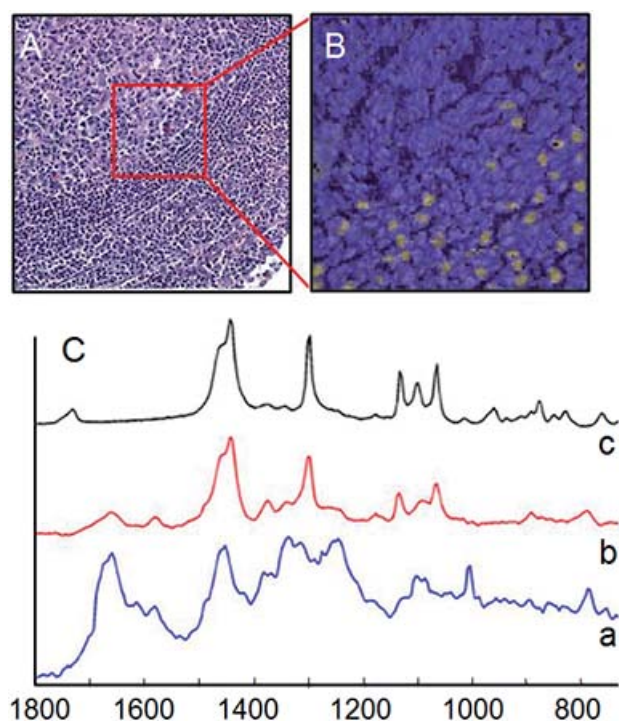


Figure 13 (A) Photomicrograph of H&E stained section of a germinal center and the mantle zone of a lymph node (see text for detail). (B) Raman SHP image, constructed via VCA (see text) showing areas of non-activated and activated lymphocytes; the nuclei of the latter being detected by VCA. (C) Endmember spectrum of cell cytoplasm and nuclei of non-activated lymphocytes (a) and endmember spectrum corresponding to yellow spots (b). A reference spectrum of phosphatidyl-choline is shown in trace (c).

would be the first foray of SHP out of the diagnostic realm into more prognostic areas, and if found to be generally true, could enormously help in prognostic and therapeutic decisions.

This is particularly so for lung cancer, where there are three types of common cancer types: small cell lung cancer (SCLC), adenocarcinoma (ADC) and squamous cell carcinoma (SqCC). When the two latter cancers are poorly differentiated (grade 3), they are difficult to distinguish in classical histopathology. Yet, the correct diagnosis is highly important, since different treatment regimens are generally called for. In 2012, we reported an 80-patient pilot study [72] to determine whether these three cancer types could be differentiated and diagnosed by SHP, based on different chemical composition and without the use of morphological criteria or advanced methods such as immunohistochemistry (IHC) or gene array technology. Since SHP is a non-destructive method that works on unstained histopathological specimens, it would offer a much reduced workflow of analysis over other methods.

4.2.2 Diagnosis of lung SqCC and lung ADC *via* IR-SHP

In this pilot study, a tissue microarray was used which contained, among other tissue types, 20 adenocarcinomas and 12 squamous cell carcinomas. These tissue cores, about 1.5 mm in diameter, were separated into a training set and a test set. For the tissue spots in the training set, IR spectral datasets were collected as discussed before, and pre-sorted *via* hierarchical cluster analysis (see Section 3.4). Subsequently, digital images of the H&E stained tissue were taken, and annotated by a lung pathologist to correlate visual tissue features (disease) and cluster memberships (see Section 3.6). This resulted in a dataset of spectra for which a detailed pathological diagnosis was available. This training dataset contained 6640 pixel spectra of SqCC and an equal number of pixel spectra of ADC,

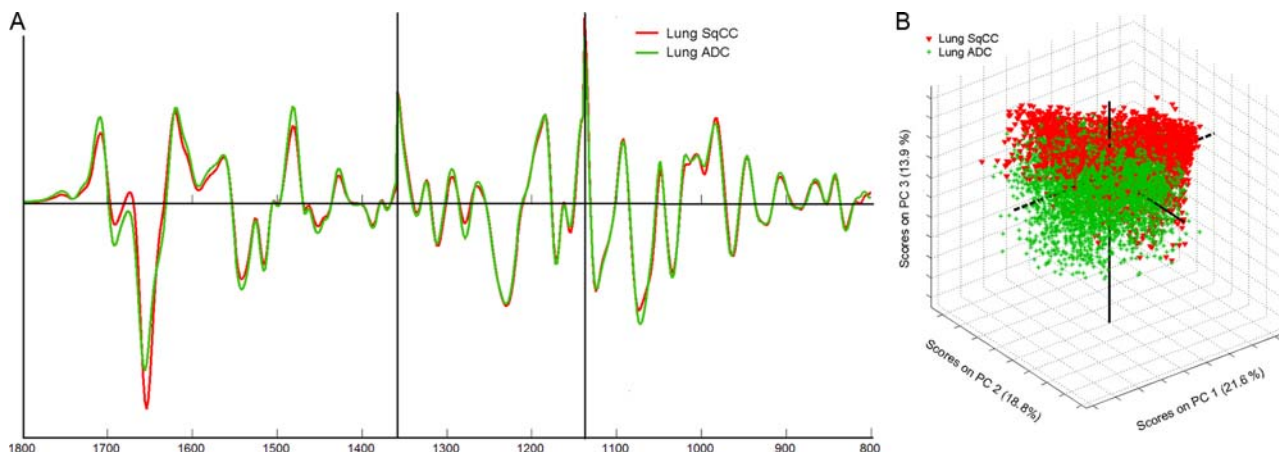


Figure 14 (A) Mean 2nd derivative spectra of lung ADC and SqCC, (B) PCA plot demonstrating the separation of the two cancer classes.

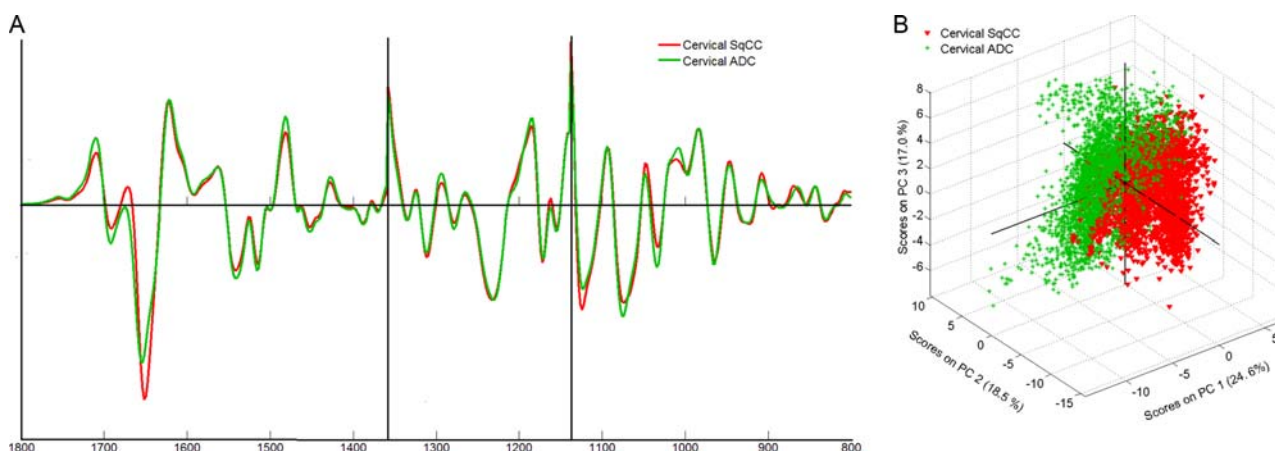


Figure 15 (A) Mean 2nd derivative spectra of cervical ADC and SqCC, (B) PCA plot demonstrating the separation of the two cancer classes.

and subsequently was used to train an artificial neural network (ANN) to analyze unknown data.

Spectral data of the tissue spots in the test sets were collected and analyzed exactly the same way the training set tissue spots were treated, and a test set of 6640 spectra was created. When this test set was analyzed by the ANN described above, a sensitivity of 90% and a specificity of 95% were obtained, indicating that there exist reproducible differences in the spectra of these cancer classes. Figure 14 shows normalized mean 2nd derivative spectra of the two classes, and although the spectral differences are small, they are sufficient for PCA or an ANN to separate the classes with high accuracy. The vertical lines in Figure 14 A delineate regions in which the spectra were normalized individually, as described in Section 4.1.2. Separate normalization of spectral regions, as indicated above, offers the advantage of de-emphasizing the protein spectral region in favor of nucleic acid contributions which is apparent in the graph since the three different regions have nearly equal spectral amplitudes. Figure 14B shows the spectral discrimination between the ADC and SqCC spectra as a PCA scores plot. We find that ANNs can distinguish spectral classes with ease if they form distinct spectral clouds *via* PCA, as shown in Figure 14B.

Recent results, both in IR and Raman SHP indicate that spectra of different tissue classes are quite similar; thus, the overall similarity of the spectra shown in Figure 14 is not surprising. In fact, when large spectral differences between cancerous and normal tissue types are reported in the literature, these differences are nearly always due to artifacts and confounding factors. Real spectral differences between tissue classes are usually found in the details, for example slight differences in the phosphodiester symmetric and antisymmetric stretching

bands at ca. 1095 and 1235 cm⁻¹, and slight changes in amide I and amide II peak intensities.

The aforementioned pilot study for lung cancer diagnostics [72] also included tissue spots with small cell carcinomas, as well as normal tissue. Discrimination of all tissue types was accomplished by training hierarchical neural networks consecutively; the order of discrimination was based on the variance in the dataset. Thus, normal and cancerous tissues types that exhibited largest differences were classified first by a top level ANN. Subsequently, the cancerous tissue types were separated into SCLC and not-SCLC by a second level ANN. Finally, among the not-SCLC class, ADC and SqCC were separated, as described above.

Since the discrimination between lung ADC and lung SqCC could be carried out by IR-SHP relatively easily and with high accuracy, the question naturally arose whether other organs in which ADC and SqCC occur show similar discrimination between the cancer types, and whether SqCC (or ADC) from different organs exhibit the same spectral pattern. To answer this question, tissue microarrays from cancers of the cervix, esophagus and stomach were obtained, and a study similar to the one described above was carried out.

4.2.3 Diagnosis of cervical SqCC and cervical ADC *via* SHP

In the following, the results obtained for cervical SqCC and ADC will be introduced; similar results were obtained for esophageal cancers as well, but the low number of sample spots does not allow us to arrive at a definitive answer at this point.

For cervical ADC and SqCC, however, we observed exactly the same trends, and very similar spectra, as for lung cancers. Although cervical ADC

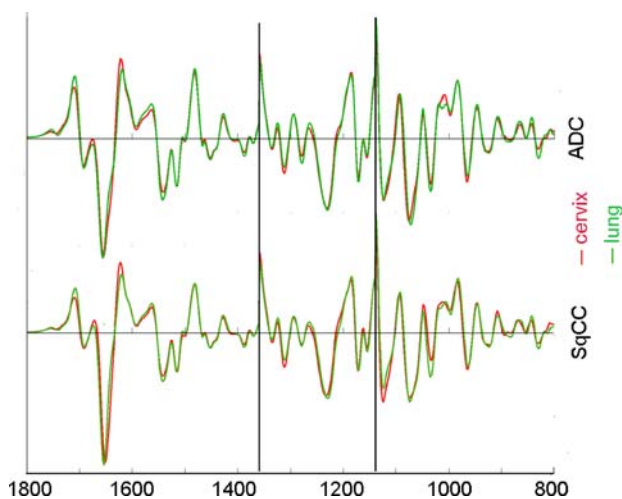


Figure 16 Comparison between spectra due to ADC and SqCC of different organs.

is very rare, we were able to secure a microarray with sufficient sample spots for detailed analysis. Figure 15 shows a plot, analogous to Figure 14, which depicts the mean 2nd derivative spectra, as well as a PCA scores plot which indicates that cervical ADC and cervical SqCC can be separated in principal component space. Similarly, an ANN was trained that discriminated ADC from SqCC with a sensitivity of 98% and a specificity of 98%¹. Thus, it appears that cervical ADC and SqCC can be distinguished with very good accuracy as well.

The remaining question, whether adenocarcinomas in different organs have similar spectra will be discussed next. Figure 16 depicts the mean 2nd derivative spectra shown before in Figures 14 and 15, but drawn to permit a direct comparison between ADC and SqCC from different organs. cursory inspection of Figure 16 reveals that all four spectra are quite similar. However, it appears that in the SqCCs of the cervical and the lung samples, the nucleic acid phosphodiester vibrations (1095 and 1235 cm⁻¹) bands are broader, and the amide I peak is narrower (in particular, the shoulder at ca. 1630 cm⁻¹ is less pronounced). Other small differences do exist but may not be obvious to the naked eye. The total number of spectra averaged and shown in Figure 16 exceeds well over 50,000, derived from over 50 patients; these spectra do not take into account different grades of the diseases. More important than finding common spectral properties of the same cancers in different organs will be the search for cancer markers in these tissues; for example, the overexpression of genes such as HER2/neu or other cancer markers. A paper

by Hartsuiker et al. [73] reported results indicating that Raman imaging of individual cells could distinguish cultured cells overexpressing this gene. In addition, a recent paper by Kallenbach et al. [77] indicated that regions of high p53 and Ki67 activity, detected *via* IHC fluorescence microscopic imaging, correlated well with regions of specific IR signatures. Thus, we may expect that SHP data, when analyzed properly, may provide information on cancer type, cancer grade, and presence of certain prognostic markers in one measurement that presently require several separate procedures (H&E, IHC), and are less subjective in nature.

4.3 Results from IR Spectral Cytopathology (SCP)

4.3.1 Background

In the last decade of the 20th century, several groups attempted to utilize IR spectroscopy as a tool to diagnose cervical disease [78–80]. The reasons for these efforts were partially due to the enormous success of several other research groups in classifying prokaryotic cells (bacteria) by IR spectral methods; the other reason was that cervical cancer screening promised a huge market because of the frequency classical cervical cytology is being performed (ca. 100 million tests/year in the US alone), and due to the relatively low overall accuracy of classical cytology.

Unfortunately, the earliest results reported (from cell pellets, rather than from individual cells) were confounded by poor sample preparation, lack of corroborating results from classical cytopathology, scattering and fixation issues, low instrument sensitivity and quite restricted computer performance. In spite of these obstacles, work by Cohnford and Rigas [81] relatively early pointed out one of the most relevant aspects of SCP, namely that most cells from an abnormal cervical sample exhibit spectra that are more closely related to the spectral patterns of diagnostic abnormal cells than to those of normal cells. This is true for cells still with normal morphology and therefore, offers the prospects of developing a test with much higher sensitivity than classical cytopathology, since more cells present abnormal properties.

At the LSpD, methods have recently developed that allow the automatic acquisition of cellular spectra from large numbers of individual cells. These developments have led to several studies which detailed application of the methodology to both cervical and oral squamous cells [23, 82–84]. Based on the success of these studies, an expanded pre-clinical trial was carried out at the LSpD, the results of which will be presented in this section.

¹ The increased accuracy of the cervical ADC vs. SqCC over the lung ADC vs. SqCC discrimination is attributed to better annotation procedures recently instituted, which produced more homogeneous datasets

4.3.2. Design and methods of the pre-clinical trial for oral screening

This oral screening pre-clinical trial was launched at Northeastern University in 2010 to accomplish two main goals: the development of robust databases of normal oral cytology samples, and to expand these databases to represent external influences such as tobacco use, medication, viral exposure, etc. In addition to 90 (presumably normal samples) from volunteers at Northeastern University, this trial included a cohort of 30 patients with oral disease. The interest in developing a screening tool for oral cancers was stimulated by the high occurrence of oral cancers in far eastern populations served by Tufts Medical Center (TMC), the clinical partner of the LSpD. Furthermore, no screening tests for oral cancers exist; thus, they often are detected at advanced stages of the disease, a fact which contributes to poor long term survival of patients with oral cancer. Finally, the high recurrence rate of oral cancers poses some interesting question whether or not SCP can detect risk factors for recurrence.

The pre-clinical trial, carried under Institutional Review Board (IRB) approval from Northeastern University, Division of Research Integrity, resulted in ca. 270 samples since three regions of the oral cavity (mouth floor, cheeks, tongue) were sampled separately. Volunteer information (age, gender, exposure to tobacco or medication, history of oral disease) was collected before sample exfoliation. Clinical samples, defined here as cell samples exfoliated from patients with dysplasia or oral cancer, were obtained from the Department of Pathology at TMC. These samples consisted nearly exclusively of cells with normal morphology collected from the vicinity of the lesion diagnosed as abnormal.

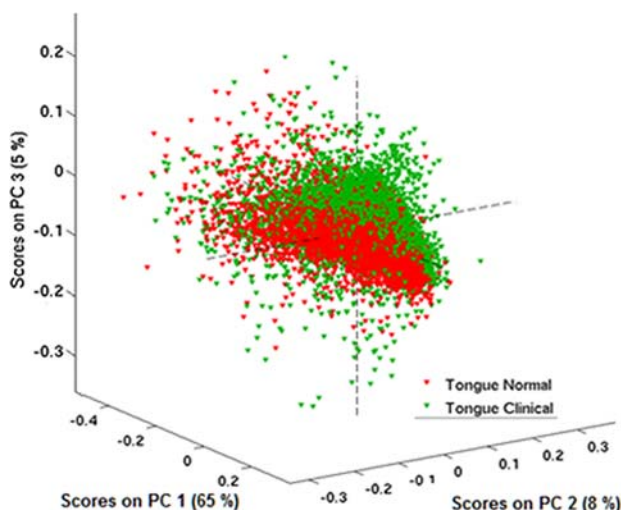


Figure 17 PCA scores plots of normal vs. clinical (see text) samples of oral mucosa cells from the tongue.

Normal oral cytology samples were collected from volunteers after the subjects rinsed their mouth with water to rid the cavity of any debris. Cells from the oral cavity were exfoliated by swabbing the three collection areas for 30 seconds using sterile cyto-brushes which were immersed immediately after sample collection into bar-coded plastic jars filled with SurePath solution (Burlington, NC USA). All clinical oral samples, collected at TMC, were split into two samples after being collected: one of these went to conventional cytological analysis, while the other samples (on cytological brushes) were stored in SurePath solution (Burlington, NC USA). All clinical samples received positive histopathological diagnoses which were available to LSpD personnel.

Volunteer and clinical samples were prepared identically, as described above, on ‘low-e’ substrates and subject to data acquisition and manipulation as described above. These procedures eventually yield one scattering and noise corrected, expanded second derivative spectrum for each cell. Typically, from one patient, between 500 and 1000 cellular spectra from each of the anatomical regions were collected and stored in a database that permitted searching against patient information such as tobacco use, disease history, etc.

Data were analyzed by unsupervised and supervised multivariate methods. Principal Component Analysis (PCA) [58] was used as an unsupervised method to determine whether or not there were systematic variations in cellular spectra. PCA results are displayed as 2- or 3-dimensional ‘scores plots’, in which each symbol represents one cell spectrum. The axis in these scores plots are the contributions (scores) of each cellular spectrum along the principal components indicated. Clustering of spectra indicates that significant variations exist in the datasets. If PCA plots showed significant differences between spectral classes, a supervised algorithm based on Artificial Neural Networks (ANNs) [58] were used to diagnose spectra from test datasets with high accuracy.

4.3.3 SCP results for the oral mucosa

Preliminary results on oral SCP from a smaller cohort of patients and volunteers were previously reported [76, 75, 84]. This study demonstrated small differences in spectral features observed for different anatomical regions of the oral cavity, and a clear differentiation between normal and cancer cells. The present study confirmed these results for larger databases. These cells cannot be distinguished morphologically; thus, SCP here offers superb and enhanced sensitivity to detect slightly different protein composition in these cell types.

Even more importantly, Figure 17 shows a scores plot of normal (red) and clinical (green) cell spectra from the tongue. Since the spectral characteristics are slightly different for cells from the cheeks, the mouth floor and the tongue, only cells exfoliated from the tongue were included in this analysis. Here, each colored dot represents one cell spectrum; in total, there were over 3900 spectra in each of the two classes. With these results, we confirmed the aforementioned finding that most of the cells from clinical samples exhibit abnormal spectral features, even if the majority of these cells exhibit normal morphology. In the past, we have reported [83] that the cells with abnormal morphology show the same spectral results as the morphologically normal cells from abnormal samples.

This observation suggests that the cells from the vicinity of cancerous lesions already exhibit biochemical changes that can be detected spectroscopically. This observation correlates to well-known, but quite ill-defined observations referred to as field cancerization or malignancy induced changes. Both these terms were coined to express the changes in cells in the vicinity of a lesion. These effects, in part, explain the high recurrence rates in oral cancers. For cervical cells, we showed [85] that one cause of the spectral similarities between dysplastic cells with abnormal morphology and morphologically normal cells from abnormal samples might be a viral infection. Cervical dysplasia, in particular, is associated in the vast majority of all cases with a concomitant infection by the *human papillomavirus* (HPV), and we [85] and others [86] have shown that such a viral infection is detectable spectroscopically.

Unsupervised analysis of spectral data by PCA does demonstrate that there exist consistent and interpretable changes between the spectra of normal and clinical samples, although they present no mechanism to use spectral data for a predictive diagnosis. Such a diagnosis is obtained best using supervised, or trained algorithms. A number of such predictive algorithms exist, some very similar to the principles of PCA (for example, Soft Independent Modeling of Class Analogy, SIMCA), linear discriminant analysis, LDA, to more complicated classi-

fiers such as Support Vector Machines, SVMs, which are based on separating spectral classes by complicated, multidimensional separation planes. At the LSpD, artificial neural networks have been used [72] for the trained prediction of class memberships.

Thus, an ANN was created with data from tongue cancer since this dataset offered the largest patient number. The aim of this ANN was to determine whether or not the small biochemical changes induced by disease allowed a supervised algorithm to distinguish these classes of spectra. Such algorithms will ultimately be used as a screening diagnostic tool in the future. Table 1 shows the results for the ANN trained with 600 spectra (300 randomly selected spectra from normal and 300 spectra from clinical samples) and tested on 800 spectra of tongue cells, 400 from normal and 400 from clinically abnormal samples. 50 (intensity) features were selected in each spectral vector *via* entropy-based feature selection, using the 'rankfeature' function in MATLAB. The MATLAB 'feedforward' ANN-function was utilized for ANN construction, employing 50 inputs (the 'features' discussed above), one hidden layer with two nodes, and one output neuron (cancer/normal). The results of this ANN, expressed in terms of sensitivity, specificity and overall accuracy, are shown in Table 1.

The results from this trained algorithm are, obviously, excellent and offer a glimpse into the sensitivity and specificity that can be achieved with the spectral methods. The overall accuracy is comparable to the results obtained in spectral histopathology (SHP) for the distinction of certain lung cancers [72]. In particular, we wish to emphasize that these results here were obtained from cells that were morphologically normal; that is, from cells that make up the vast majority in exfoliated cell samples. The observations reported here re-emphasize the fact that changes in biochemical composition of abnormal cells occur before they change morphology.

The dataset of oral cells is presently being further analyzed to detect any other possible effect on oral mucosa cells. Interestingly, we found for example, that there was a slight difference in the cells collected from women using oral contraceptives, and those who don't. We had observed and reported similar findings previously [83] for cervical cells. In this case, the dependence of cell maturation on hormonal levels is well established. In order to account for the changes exhibited by cell spectra over the menstrual cycle, only women using oral contraceptives were included in our original studies on SCP of cervical samples. Thus, the change of oral mucosal cells between women using oral contraceptives, and those who don't, does not come as a complete surprise, in particular, since it is well established that oral mucosa cells do express the estrogen receptor.

Table 1 Sensitivity, specificity and accuracy of the ANN trained to distinguish normal and clinical samples of tongue cancer.

		Classical Cytopathology	
		Positive	Negative
Spectral cytopathology	Positive	384 (48%)	23 (2.9%)
	Negative	16 (2.0)	377 (47.1%)

Accuracy 95.1% Sensitivity 96% Specificity 95.1%

4.3.4 SCP results for the cervical mucosa

LSpD results from these studies have been reported in the literature before [82, 83, 85]. Our earliest reports dealt with the spectral changes in exfoliated cervical cells due to the hormonal changes associated with menopause [82]. These results were still based on a previous method of data acquisition, which was less automated and much more labor intensive. Therefore, the datasets in this study are much smaller than the present ones, yet it became obvious that the hormonal changes in cell spectra had to be taken into account. This became even more obvious when spectra from samples collected early, in the middle and toward the end of the menstrual cycle. In order to avoid mixing hormonal effects with those due to cervical disease, all subsequent SCP studies were carried out using samples from women using oral contraceptives which keep the hormonal level more constant. The cell spectra of women using oral contraceptives clustered with those of mid-cycle samples.

Subsequent to these efforts, a larger study from 17 women was carried out in which basically the same results observed for oral mucosa was reproduced, namely that all cells from abnormal samples showed abnormal spectra, even when still morphologically normal. Furthermore, we showed in this study that the spectra of the few cells with abnormal morphology coincided with those of the morphologically still normal cells [83, 85].

In this study, we also observed that spectral abnormality may persist even after treatment, or when subsequent cervical examinations proclaimed the patient to be free of disease. We attributed this persistence of spectral abnormality to viral infection; indeed, it appears that the spectral changes observed in SCP may be partially due to infection by HPV. To shed further light onto this possibility, a study was carried out involving 49 clinical cervical samples all of which were tested for HPV infection *via* the Digene hybrid test for high risk HPV (hrHPV) strain. The SCP results were analyzed with a trained algorithm (SIMCA, see above) and produced good sensitivity (only one hrHPV sample was missed) but poor specificity. The low specificity was attributed to the fact that no low risk (lrHPV) information was provided; thus, it is entirely possible that the false positive SCP results were due with sample infected by lrHPV [85]. This infection is about as common as high risk infection, and might induce spectral changes in the cells that mirror those of hrHPV infection.

These efforts were accompanied by model system studies in which cultured cervical cells infected with a different number of copies of the virus were compared. Similar Raman SCP results on cervical tissue were published at about the same time [86, 87]. Our IR SCP results strongly suggest that a change in the

total proteome of cells is observed when the virus infects a cell. Since the cell's protein expression is reprogrammed by the virus, it is not surprising that these changes can be detected by SCP.

4.4 IR and Raman-SHP of brain metastases

Brain metastases occur in about 15–40% of all cancer patients [88]. In up to 15% of all cases, the primary tumor of brain metastases remains unknown despite thorough investigation by standard screening techniques. The diagnosis is called “cancer of unknown primary”. The failure to detect the primary tumor is usually due to its small size and lack of symptoms, and constitutes the main problem to select an organ-specific therapy. Lung carcinoma which is known to cause thoracic symptoms in a fairly late stage of tumor development is the most frequent site for brain metastases. Other frequent primary tumors are colorectal cancer, breast carcinoma, renal cell carcinoma, prostate cancer and malignant melanoma. The concept to apply vibrational spectroscopy to identify the primary tumor is that metastatic tumor cells contain molecular information of the primary tumor and vibrational spectra provide a molecular fingerprint of the tissue type which may enable its assignment by a supervised classification model. This was demonstrated for the first time for FTIR images of 20 human specimens [71, 89]. In these studies, $4 \times 4 \text{ mm}^2$ FTIR images were collected with a resolution of $62 \times 62 \text{ }\mu\text{m}$ per pixel. The data were classified by linear discriminant analysis (LDA) or soft independent modeling of class analogies. Another example was a murine model where brain metastases were induced by injection of tumor cells of malignant melanoma into the carotid artery. A fiber optic probe Raman setup was applied to collect Raman images of murine brains [90] and brain regions in living mice through a cranial window [91]. Recent work studied human brain metastases by Raman and FTIR microscopic imaging [92, 93]. Here, an analogous strategy was applied as shown in Figure 5. First, HCA was performed to annotate the spectra using reference information from histopathology. Then, a hierarchical classification approach was developed to distinguish the carcinoma spectra from the other spectra in a first level and determine the primary tumor of the brain metastasis in a second level. Before this approach is summarized in Section 4.4.2, typical IR and Raman spectra of brain tissue and brain metastases are presented.

4.4.1 IR and Raman spectra of brain tissue

IR and Raman spectra of brain tissue, necrosis, and brain metastases of lung carcinoma and renal cell

are shown in Figure 18. The un-derivatized IR spectra are normalized to the amide I band at 1655 cm^{-1} . Then, the other protein bands show almost no variations (amide II at 1544 and amide A at 3300 cm^{-1}). As normal brain is a tissue type with high lipid content, lipid bands at 1059 , 1080 , 1237 , 1466 , 1736 , 2852 and 2922 cm^{-1} are intense. Their intensities are smaller in necrotic tissue and significantly lower in brain metastases which constitute the main discriminant spectral feature between normal and pathological tissue. Another spectral marker is glycogen in brain metastases of renal cell carcinoma with typical bands near 1030 , 1080 , 1151 and 3400 cm^{-1} . The spectral markers in brain metastases of lung carcinoma (red trace) and other brain metastases (not shown) are less evident. But they exist and allow to determine the primary tumor as shown below.

The Raman spectra qualitatively agree with the IR spectra although the spectral contributions differ quantitatively. Most intense lipid bands in normal brain tissue are found at 701 (cholesterol), 718 , 1063 , 1127 , 1268 , 1298 , 1439 , 1657 , 2850 , 2882 and 2926 cm^{-1} . The shaded regions show the variations of the 16th and 84th percentile. It is interesting to note that the variations occur near 1268 and 1657 cm^{-1} are assigned to unsaturated fatty acids moieties in li-

pids. Lipid bands decrease in necrotic tissue relative to protein bands that are resolved at 622 , 643 , 757 , 828 , 851 , 1003 , 1032 , 1208 , 1240 , 1450 and 1668 cm^{-1} . The most significant variations in the 16th and 84th percentile occur near 739 , 1250 and 1585 cm^{-1} that are assigned to hemoglobin in hemorrhage. Generally, Raman bands have narrower widths than their IR counterparts. The Raman spectra of lung carcinoma and renal cell carcinoma metastases have slightly higher lipid bands than necrotic tissue, but still less intense than normal tissue. In addition, spectral contributions at 855 , 940 and 1340 cm^{-1} are more intense in renal cell carcinoma relative to protein bands. These bands indicate increased glycogen content. A comparison between Raman and IR spectra clearly demonstrates their complimentary nature. Some bands are only visible in IR spectra (such as protein amide II) and some bands only in Raman spectra (protein band at 1003 cm^{-1}). Spectral contributions of heme groups are enhanced in Raman spectra due to a pre-resonance effect. Spectral contributions of OH groups in carbohydrates such as glycogen are more intense in IR spectra due to their strong dipole moment. More details about the theory and band assignments were given in a recent tutorial [94].

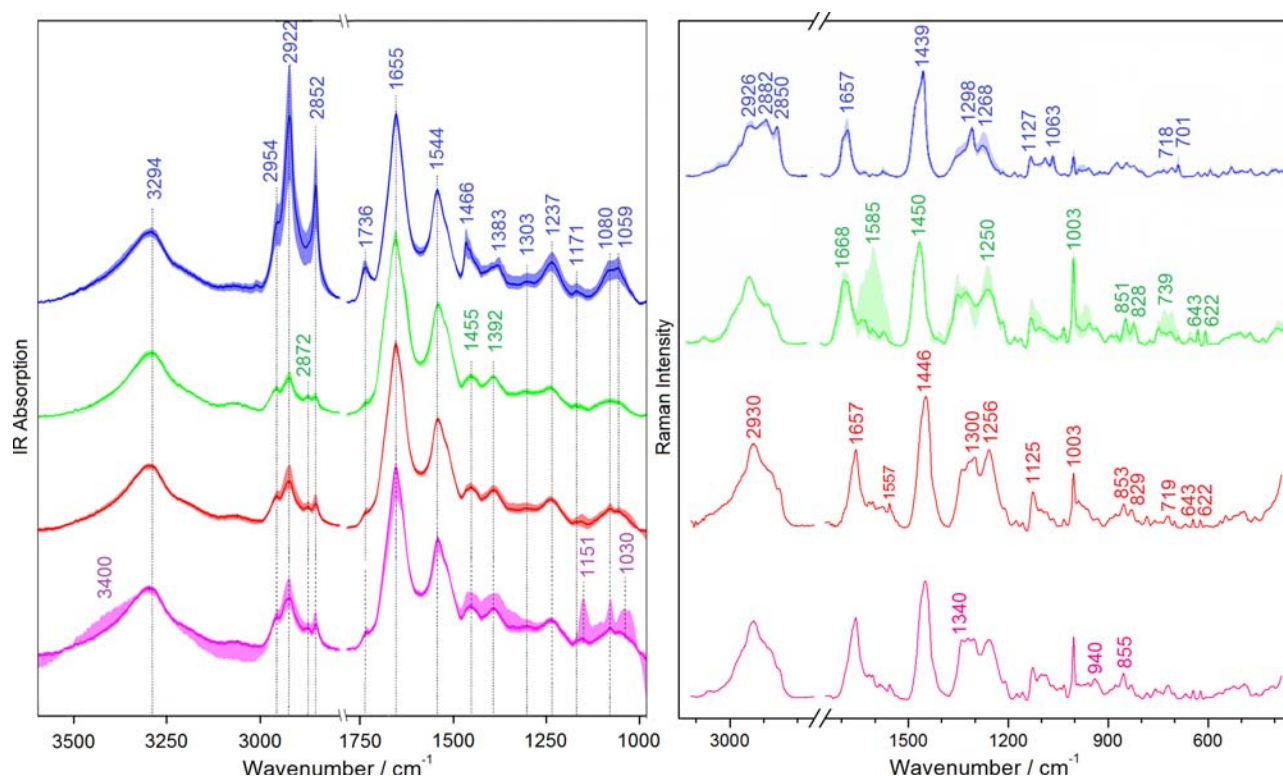


Figure 18 IR spectra (left) and Raman spectra (right) of normal brain tissue (blue trace), necrosis (green), brain metastasis of lung carcinoma (red) and renal cell carcinoma (magenta). Shaded regions display the 14th and 86th percentile.

4.4.2 Identification of tumor margins

In contrast to the most frequent primary brain tumors, gliomas which exhibit diffuse, infiltrative growth, brain metastases are characterized by well-defined tumor margins. During neurosurgery it is of utmost importance to identify the tumor margin as the scope is to maximize tumor resection upon minimal removal of normal brain tissue and preservation of brain function. In the context of histopathological assessment of brain metastasis the carcinoma portion of the tissue section is identified as the underlying spectra diagnostic of the primary tumor. Spectra from other tissues such as normal brain, hemorrhage or necrosis are less informative for the determination of the primary tumor.

The strategy follows the route outlined in Figure 5. Training images are segmented by cluster analysis and the groups are annotated using reference information from the gold standard (histopathological inspection) of the stained tissue section after data acquisition. These data are used to train a diagnostic classification algorithm that can be subjected to independent, unknown data. In a hierarchical fashion, first carcinoma spectra are separated from non-carcinoma spectra because the spectral variations between brain metastases originating from different primary tumors are smaller than between carcinoma, normal brain, hemorrhage and necrosis as shown in the previous section. Examples are given in Figure 19 for a brain metastasis of lung carcinoma. The H & E stained tissue section adjacent to the unstained section reveals carcinoma, necrosis, carcinoma islets and scattered tumor cells. A recent study encompassed 17 specimens [92] that served as training data for support vector machines (SVM) for tissue recognition. The reclassification is included in Figure 19 for the Raman image (b) and FTIR image (d). The Raman image contains 61×61 spectra at the step size of $10 \mu\text{m}$. The FTIR image is composed of a mosaic of 3×2 images of $350 \times 350 \mu\text{m}^2$ each totaling to an area of $1050 \times 700 \mu\text{m}^2$. Each FTIR pixel correspond to an area of $5.5 \times 5.5 \mu\text{m}^2$. Both Raman and FTIR images distinguish tumor (red), from necrosis (green) and remaining regions (black) that represent mainly regions without tissue in holes or cracks. The scattered red pixels within the green area are consistent with scattered tumor cells in necrosis as evident from comparison with the H & E stained tissue. These scattered tumor cells are not resolved in the FTIR image probably due to the lower lateral resolution. Normal brain (blue) has not been recognized in either image which is consistent with the absence of such tissue.

The correct predicted values (CPV) were calculated by comparing the SVM assignments with the cluster annotations. The overall CPVs of the defined

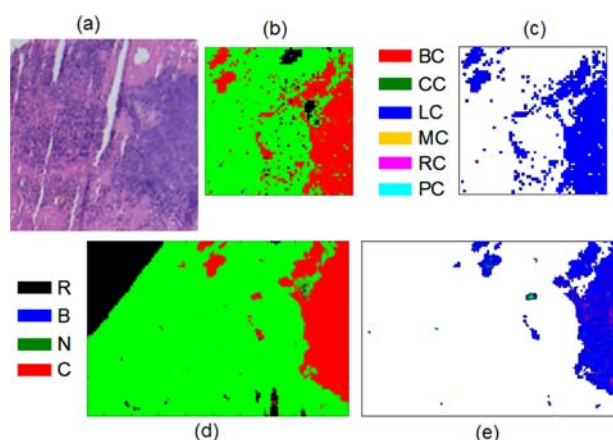


Figure 19 H & E stained tissue section (a), Raman images (b, c) and FTIR images (d, e) of brain metastases of lung carcinoma. Panels (b, d) distinguish carcinoma (C), necrosis (N), normal brain (B) and remaining (R), panels (c, e) assign the primary tumor to bladder carcinoma (BC), colon carcinoma (CC), lung carcinoma (LC), mamma carcinoma (MC), renal cell carcinoma (RC) and prostate carcinoma (PC).

tissue types (normal, carcinoma, necrosis and remaining) were 96.3% for Raman images and 96.7% for FTIR images using 17 specimens as training data.

4.4.3 Determination of primary tumor

The study encompassed brain metastases of bladder cancer, colon cancer, lung carcinoma, mamma carcinoma, renal cell carcinoma and prostate carcinoma [92]. A second SVM was trained for primary tumor recognition using the carcinoma spectra from the first SVM as input. The color-coded results are included in Figure 19. 1072 out of 1078 Raman spectra (99.4%) and 97.8% of the IR spectra were assigned to the primary tumor lung carcinoma. The agreement is remarkable as the initial histopathologic diagnosis was carcinoma of unknown primary with a suspected lung carcinoma. The Raman and IR results confirm this diagnosis.

Again, CPVs were calculated for the recognition of six primary tumors. The overall CPVs were 99.8% and 96.9% for Raman and FTIR images, respectively, using 17 specimens as training data. If the criterion is applied that the majority of spectra determines the primary tumor then all specimens were correctly predicted.

This also holds true for four independent specimens used for validation. The data were preprocessed in the same way than the training data. The images were subjected to the first level SVM for carcinoma identification and the second level for primary tumor determination. The CPVs of the first lev-

el dropped to 84.4% and 87.1% for FTIR and Raman images, respectively. The CPVs of the second level dropped to 64.8% and 89.3% for independent FTIR and Raman images, respectively. The good agreement and the high values suggest that Raman and IR imaging probe the tissue-specific biochemical fingerprint and can identify tumor type. Small deviations observed for independent specimens might be due to different specimens used for validation. The main difference between Raman and IR spectroscopy is the acquisition time and suitability to sample preparation: IR images of more than 4000 spectra can be acquired within minutes using focal plane array detectors, whereas it is more time consuming to collect a comparable Raman image in a serial mapping mode. At an exposure time of 1 second per spectrum it takes more than one hour to collect 4000 spectra. Samples are usually prepared as dried tissue sections on IR-transparent substrates for FTIR imaging. These samples can also be investigated by Raman imaging. Furthermore, Raman images can be recorded from non-dried biopsies and even under real-time *in vivo* situations. These properties are utilized in the next section for the detection of tumor cells.

4.5 Raman-SCP of circulating tumor cells

Tumors can occur in almost any tissue of the body. Once a tumor is formed, it can invade the surrounding tissue and disseminate cells *via* the blood and lymph vessels all over the body. Detection and quantitation of these so called circulating tumor cells (CTC) would be a valuable diagnostic tool as it is of high diagnostic interest to separate and differentiate the tumor cells from the healthy cells in peripheral blood in order to monitor tumor spreading, assess

success of chemotherapeutic treatment and characterize the parental tumor. Currently, intensive research is performed to detect these small number of tumor cells in blood. It is assumed that only one out of 10^3 to 10^7 normal blood cells is a tumor cell. Recent approaches for the detection of CTCs include polymerase chain reaction, flow cytometry and immunohistochemistry. However, these established cell detection and characterization techniques are not yet sufficient to fulfill this demand. Furthermore, they cause high instrumental costs, are labor-intensive and time-consuming. Before Raman spectroscopy is combined with optical traps and microfluidics for cell sorting, the principle of Raman-based cell identification was demonstrated for dried cells and cells in optical tweezers.

4.5.1 Dried cells

Using Raman micro-spectroscopy, detailed biochemical information of individual cells can be obtained with a spatial resolution in the sub-micrometer range. The Raman spectra of cells appear very complex because the contributions of numerous biological molecules such as proteins, nucleic acids, lipids and carbohydrates overlap giving a sensitive and specific fingerprint. As various cell types differ in molecular composition and structure, they also differ in their Raman spectra. Multivariate statistical algorithms are often necessary to extract these minor spectral changes from the complex Raman spectra and use them for classification. Rather than searching for rare CTCs, a model system was constructed which consists of leukocytes extracted from blood of tumor-free patients, and cultured tumor cells from acute myeloid leukemia (OCI-AML3) and breast cancer (MCF7 and BT20). The cells were fixed in

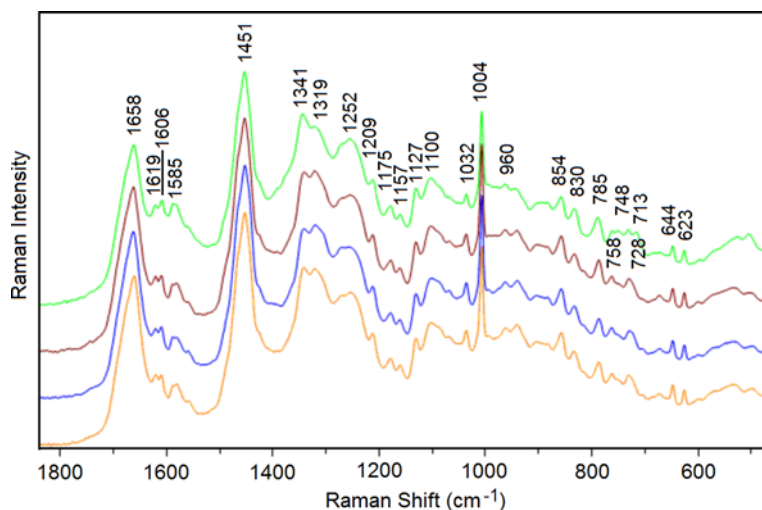


Figure 20 Raman spectra of dried cells on CaF_2 . Green trace: leukocytes, brown: OCI-AML3, blue: BT20, orange: MCF7.

paraformaldehyde, transferred onto calcium fluoride slides and dried [95]. A near IR laser emitting at 785 nm was applied to excite the Raman spectra of single cells to reduce photodegradation and intrinsic fluorescence that overlaps with the weak Raman signals and disturbed the spectra. Raman images were collected at a step size of 1 μm . Raman spectra from each individual cell were averaged and are compared in Figure 20. Labeled bands are assigned to the protein backbone (960, 1252, 1658 cm^{-1}), aromatic amino acids (623, 644, 758, 830, 854, 1004, 1157, 1175, 1209, 1585, 1606 and 1619 cm^{-1}), aliphatic amino acids (1127, 1319, 1341, and 1451 cm^{-1}) and nucleic acids (728, 785, and 1100 cm^{-1}). More detailed assignments are given in the Ref. [95].

48 Raman images (20 leukocytes, 8 OCI-AML3, 9 MCF7 and 11 BT20) were used to train a classification model using SVMs. As the spectra were not averaged, the total data set contained 3919 spectra. The model was validated using a tenfold cross validation, where the dataset is split into ten parts (folds) and every part is predicted by a model built with the rest. Overall, 3910 spectra were correctly classified giving a prediction accuracy of more than 99.7%.

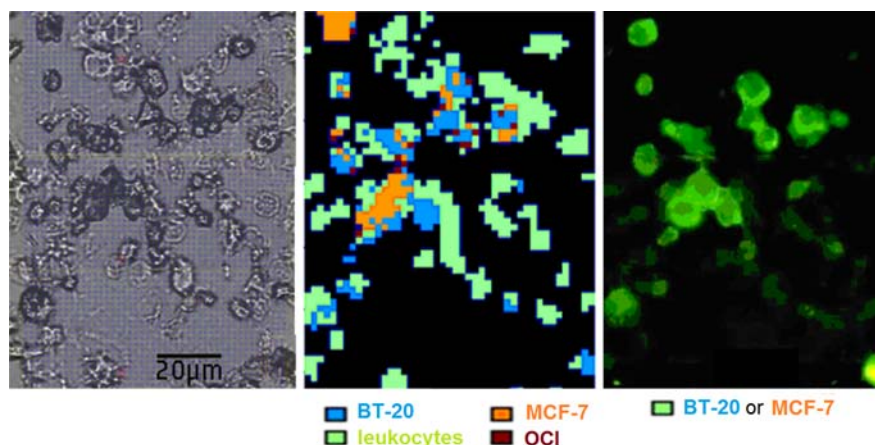
This robust model was applied to the independent sample of the mixed cell population. As an independent sample for validation, leukocytes, MCF7, BT20 and OCI-AML3 cells were mixed in a ratio 1:1:1:1. The Raman data from the mixed sample were processed in the same way and subjected to the SVM model. The color-coded classification results are shown in Figure 21. MCF7 and BT20 cells on the mixed slide were identified with a FITC-conjugated EpCAM antibody. EpCAM is a cell surface molecule which is characteristic for epithelial cells from which the MCF7 and BT20 tumor cells originate. The FITC fluorescence image was compared with the Raman-based classification. In contrast to the fluorescence image, BT20 and MCF7 cells were distinguished and FITC-negative leukocytes were visible in the Raman image.

4.5.2 Tweezed cells in buffer

Raman spectroscopy and optical tweezers are two compatible techniques because the laser used for Raman excitation and the high numerical microscope objective used for laser focusing and signal collection simultaneously form an optical tweezer. This arrangement also ensures that the cells remain in the focus of the laser during the time of Raman measurement. This results in optimum excitation and collection of scattered light, and subsequently in a high quality Raman spectrum of the trapped cell. However, only a single Raman spectrum instead of a Raman image can be collected in this configuration as the cell will stay with its center of gravity in the laser focus. It can be assumed that the nucleus, as the densest portion of the cell, is forced into the focus and contributes significantly to the Raman spectrum. Laser tweezers Raman spectroscopy was recently reviewed [96]. The same five cell types described in the previous section plus erythrocytes (red blood cells) were studied in PBS buffer after fixation with paraformaldehyde: 306 leukocytes and 126 erythrocytes from three different donors, 261 OCI-AML3, 301 MCF7 and 216 BT20 cells [17]. Cells were prepared from three independent cultivation batches and Raman spectra were collected on five consecutive days. Typical experimental conditions used a 785 nm single mode laser (Toptica, Germany), an upright Raman microscope (Microprobe, Kaiser Optical Systems, USA) with a 60 \times /NA 1.0 water immersion objective (Nikon, Japan), 75 mW intensity at the sample and 10 seconds exposure time. Average Raman spectra are shown in Figure 22.

Apart from the spectral contributions of water near 1630 cm^{-1} Raman spectra of cells were very similar to the spectra of dried cells in Figure 20. Main bands are assigned to the amide I band around 1657 cm^{-1} that overlaps with the broad water band, CH deformation modes of almost all cellular compo-

Figure 21 Photomicrograph (left), Raman image with color-coded classification (middle) and fluorescence image after staining with FITC-conjugated EpCAM antibody.



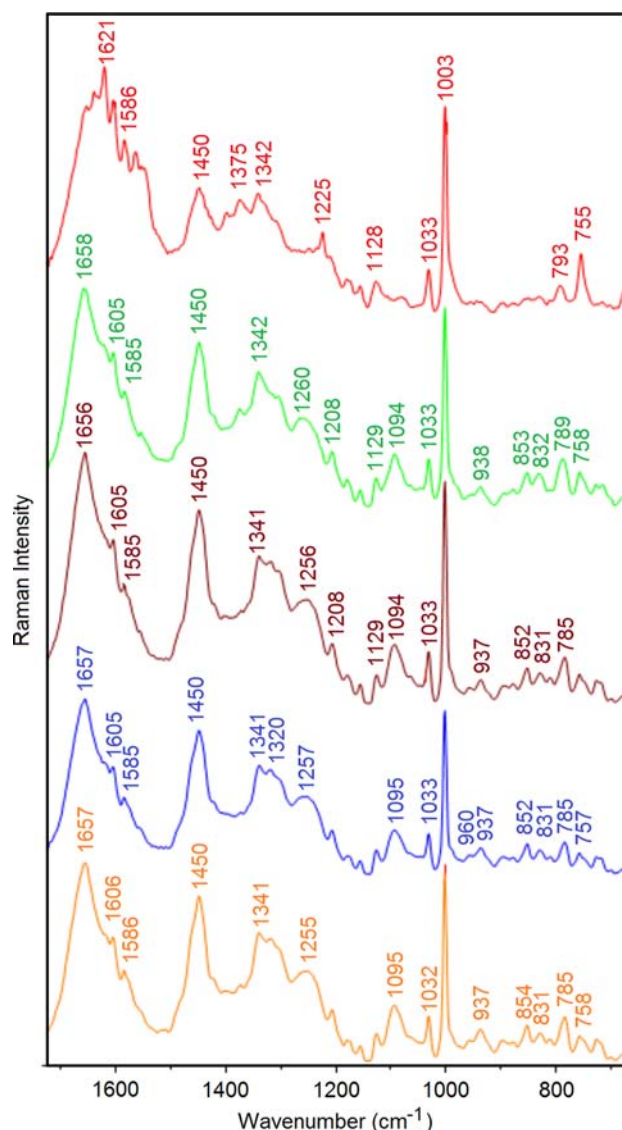


Figure 22 Raman spectra of tweezed cells in buffer. Red trace: erythrocytes, green: leukocytes, brown: OCI-AML3, blue: BT20, orange: MCF7.

nents around 1450 cm^{-1} , vibrational bands of aromatic amino acids (Phe 1605 , 1033 and 1003 cm^{-1} , Tyr 852 and 831 cm^{-1} , and Trp 758 cm^{-1}). More CH deformation modes show up around 1341 and 1320 cm^{-1} . Nucleic acid contributions are evident near 1580 , 785 and 1094 cm^{-1} whereas the latter band due to phosphodiester linkage backbone vibrations was found at 1100 cm^{-1} in dried cells as a consequence of dehydration induced denaturation. The Raman spectrum of erythrocytes looks remarkably different. This is due to the hemoglobin content which gives rise to prominent sharp bands around 1621 , 1586 , 1564 , 1374 , 1225 and 755 cm^{-1} . Even though erythrocytes can easily be distinguished from cancer cells they have not been excluded from the

data analysis as they are likely to be present in future samples from patients.

When support vector machines were trained with 1210 spectra, high sensitivity ($>99.7\%$) and specificity ($>99.5\%$) were reached to distinguish normal and cancer cells. The prediction accuracies were obtained by tenfold cross validation that means the data set was split into ten subsets, a classification model is trained with nine subsets and the tenth subset is used to predict the accuracy. Furthermore, more than 92% cells were assigned to the correct cell type which is consistent with the potential of Raman spectroscopy to determine the origin of cancer cells as shown before for brain metastases.

4.5.3 Trapped cells in microfluidic chips

In contrast to optical tweezers, two counter propagating lasers make up two-beam optical traps. Advantages of these optical traps are the drastically reduced power density inside the dielectric objects and additional scattering forces that stabilize the particle inside the trap. If the dielectric particle is a biological cell, the high local intensities in the focus of optical tweezers harbor the risk to induce unwanted cell damages. In the context of Raman spectroscopy, optical traps offer the possibility to hold and maneuver the cell relative to the excitation laser. An early study demonstrated this capability to collect Raman spectra of the cell nucleus, the cytoplasm and the membrane [97]. After non-destructive Raman-based identification cells can be sorted and subjected to further experiments. Integrated optofluidic platforms for Raman activated cell sorting (RACS) have already been proposed [98] and realized [16]. If fiber lasers with an emission at 1070 nm are used to trap the cells, almost no overlap is found with the Raman signals upon 785 nm excitation.

A dedicated microfluidic quartz chip was developed which incorporates three main operation units: a flow focusing unit for injecting single cells from a reservoir, the optical trap structure for single cell Raman spectroscopy, and a Y shaped branching unit for flow switching and cell sorting between the two chip outlets (Figure 23). Four channels accommodate the laser fibers for trapping. Additional channels were integrated for rinsing with cleaning solvents and filling with immersion fluid. The fiber channels had a diameter of $130\text{ }\mu\text{m}$ and the fluidic channels had a width of $70\text{ }\mu\text{m}$ and a height of $50\text{ }\mu\text{m}$. The chip was mounted in a holder that provides simple, accurate and stable adjustment of chip, microfluidic connections and the trapping laser fibers. Quartz has been chosen for the microfluidic chip fabrication due to its favorable optical properties compared with glass and polymers such as PDMS that generate

stronger Raman signals. First samples were the four cell types of the circulating tumor cell model (leukocytes, OCI-AML3, MCF7, BT20) studied by laser tweezing Raman spectroscopy before. The Raman chip was installed at the same Raman instrument as described above (Microprobe from Kaiser Optical Systems, USA, and single mode laser from Toptica, Germany). The acquisition time was 10 s per spectrum using 100 mW laser intensity at 785 nm. 405 cell spectra were collected (100 leukocytes, 104 BT20, 100 MCF7, 101 OCI-AML3). 21 spectra were collected without cells and used for background compensation. Figure 23 shows a single raw spectrum and processed spectra after background and baseline subtraction. The pump radiation for the 1070 nm trapping laser (963 nm corresponding to 2354 cm^{-1}) is evident as the most intense band. In spite of short-pass filters, the emission of the trapping lasers overlaps with the Raman signals above 2000 cm^{-1} . Therefore, the spectral range was cut to $650\text{--}1800\text{ cm}^{-1}$ for further processing. One additional broad, less intense band from the trapping lasers can be found at 1550 cm^{-1} . Quartz bands of the chip substrate are visible at 430, 780 and 1050 cm^{-1} . Raman bands of the cell can be identified easier after processing. The labeled bands grossly agree

with the positions of dried and tweezed cells. The shaded regions were excluded from classification and validation due to residual quartz and trapping laser contributions. Cells were identified based on Raman spectra by the classification algorithm linear discriminant analysis. Mean sensitivity and specificity determined by iterated 10-fold cross validation were 96% and 99% for the distinction of cells.

If the classification is synchronized with the micro flow control, an automated Raman activated single cell sorting will become possible. Complete automation involves cell injection, detection, trapping, spectra acquisition, data processing, classification according to a model, and cell sorting. Although the current approach with 10 s exposure time per spectrum constituted a significant progress in terms of cell number and sensitivity compared to earlier work with 120 s per spectrum, the throughput is still too low for clinical cell sorting applications. Further innovations are required to achieve higher cell sorting rates and complement the widely applied fluorescence activated cell sorting. These innovations might include shorter exposure times due to Raman signal enhancement and parallel detection channels. Slight spectral changes indicate the requirement to train individual models for each setup.

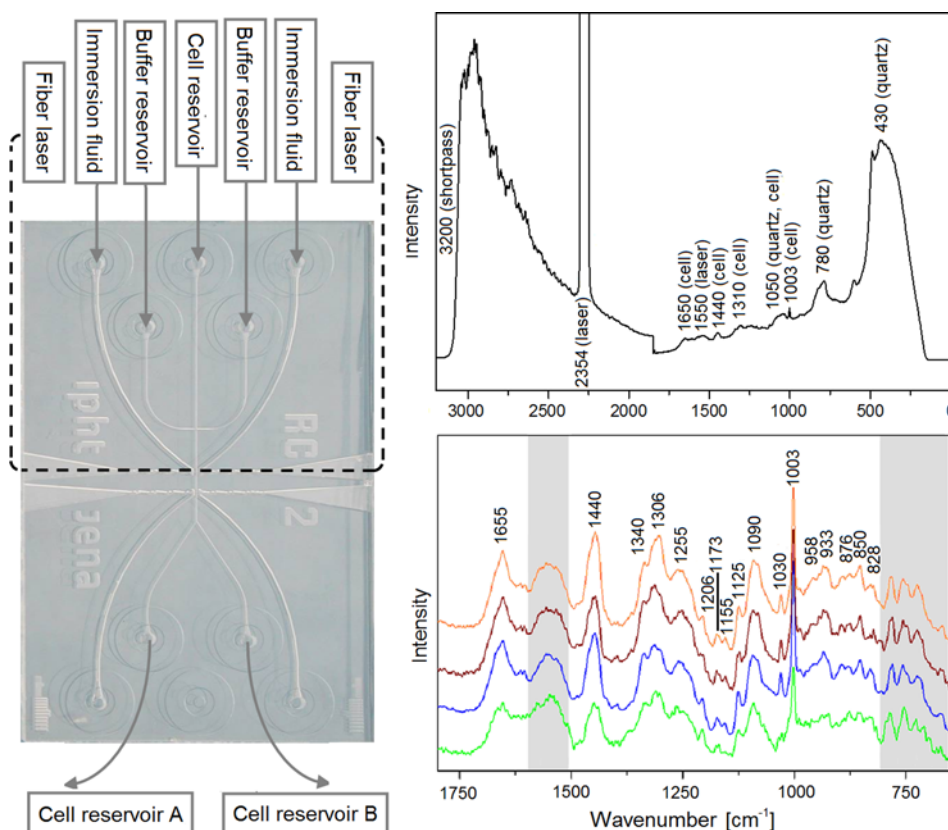


Figure 23 Scheme of Raman chip made of quartz with channel assignments (left). Unprocessed (top, right) and processed (bottom, right) Raman spectra of optically trapped, single cells in quartz chip.

4.6 High resolution confocal Raman imaging of individual cells

The last section presented here introduces another aspect of spectroscopic imaging technology that was developed during the past few years [34, 35]. This method uses Raman micro-spectroscopy of cells, in a way similar to that described in Section 4.5, but at a much higher spatial resolution. As discussed before, the best spatial resolution that can be obtained in far-field optical microscopy is determined by the wavelength of the exciting laser, and the numerical aperture (NA) of the microscope objective. Using a blue laser for excitation, and a water immersion object with a NA of 1, the spot from which the Raman spectra are collected measures ca. 300 nm in diameter. By raster scanning a cell immersed in buffer or cell culture medium through the laser spot in steps of between 300 nm and 500 nm, a hyperspectral Raman dataset can be acquired that can be analyzed by the same multivariate methods discussed before (see Section 3). Collection of such a hyperspectral dataset can be quite time consuming, since for a large cell, typically 100×100 voxel spectra are collected. Typical data acquisition times for one spectrum range from 200–500 msec, such that the collection of an entire dataset might require nearly an hour. This imaging modality produces confocal images of cells with similar spatial resolution than that afforded by confocal fluorescence microscopy, but does not require incubation of the cells with dyes or labels. Thus, the images produced are due to the natural spectral contrast of the different cellular compartments. Confocal Raman imaging also allows “depth” (X–Z or Y–Z) scans to be performed in which depth resolved spectra are collected; thus, it is possible to construct three-dimensional images based on Raman micro-spectroscopy.

This is illustrated in Figure 24, which shows pseudo-color images of a squamous epithelial cell in an aqueous environment. Panel (a) represents a univariate image constructed from a Raman hyperspectral dataset consisting of 10,000 individual spectra, collected on a 500 nm grid. The image in Figure 24a was obtained by integrating the entire C–H stretching region ($2800\text{--}3050\text{ cm}^{-1}$) and representing the integrated areas by a color scale in which yellow indicates highest and black lowest values. Obviously, this image conveys nothing but the overall shape of the cell, and the location of the nucleus.

However, when HCA is carried out on the dataset, and the results are converted to a pseudo-color image (Figure 24b), chemical information, coded in the Raman spectra, provides the imaging contrast. Here, the nucleus is shown in grey, and the chemical composition encoded in these voxel spectra is sufficiently different from that of the cytoplasm to be de-

tectable. The areas coded in red in Figure 24b are due to phospholipid inclusions which differ spectrally from the spectra of the cytoplasm, which are dominated by protein features. Figure 24c shows a confocal cross section of the cell, taken along the black line in Figure 24a. Again, the nucleus is readily discernible in this image [99].

In other studies, this methodology was used to distinguish the nucleus, the nucleoli, mitochondria-rich and membrane-rich structures inside cells without the use of any contrast agents or dyes [34]. Yet, the most important application of this technology is to monitor transport processes into cells [100, 101], for example, the uptake of drug-loaded nanoparticles. Here, the inherent chemical differences between the cytoplasm and the nanoparticle provide the imaging contrast. In previous experiments using fluorescence microscopy to follow the uptake of nanoparticles into cells, dyes as labels needed to be incorporated in the nanoparticles for their detection.

We have used confocal Raman imaging to monitor the uptake of liposomes and drug-loaded liposomes and several other nanocarriers into cells [102]. Here, we wish to report results of the uptake of complex, targeted and drug-loaded nanoparticles. The nanoparticles were composed of polymer/drug mixture (10:1 by mass). The polymer was pegylated PLGA-PCL, and the drug a pro-apoptotic ceramide. The nanoparticles carried on their surface a 17 amino acid peptide which facilitates binding to the EGF receptor of cells. The nanoparticles material exhibits an ester linkage with a prominent Raman band at ca. 1745 cm^{-1} . The drug used was deuterated at the side chain (see Figure 25D); the C–D bonds exhibit distinct peaks in the Raman spectra in a region totally devoid of other signals. The results in Figure 25 demonstrate the power of this label-free imaging technique. After an incubation time of ca. 1 hour,

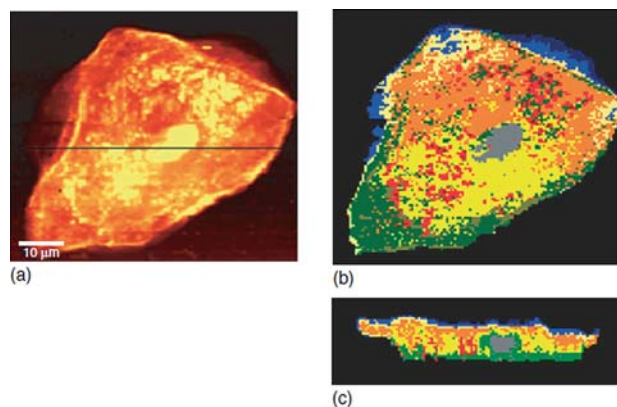


Figure 24 (a) Image of integrated C–H Raman stretching intensities of an oral mucosa cell. Brighter yellow hues correspond to higher intensities. (b) Pseudo-color image created by HCA of the same dataset. (c) Pseudo-color image of a depth scan along the black line in Panel (a).

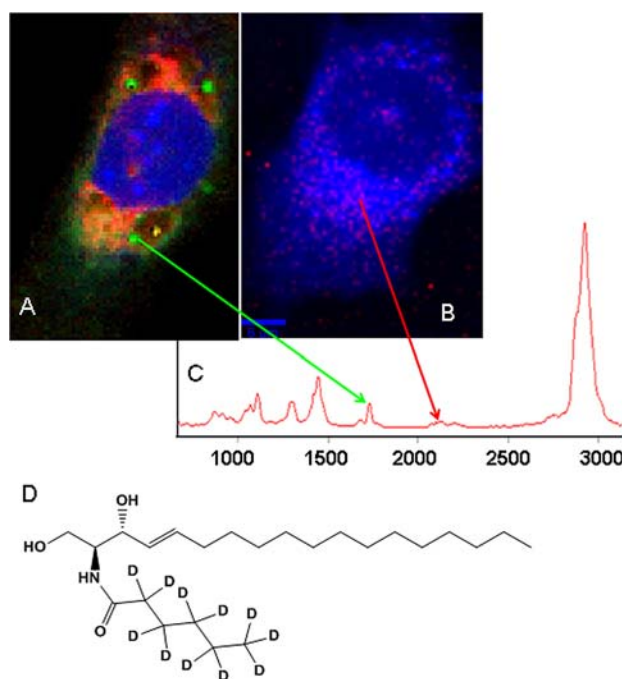


Figure 25 VCA-based Raman images of uptake of drug-loaded nanoparticles into cells. (A) early uptake shows intact nanoparticles, identified by their ester band, inside cytoplasm. (B) A later image shows the released drug, identified by the C–D stretching vibrations (C) Raman spectrum of drug-loaded nanoparticle (D) Structure of the deuterated ceramide drug.

the nanoparticles can be detected inside the cell (Panel A). The EGFR-specific peptide on the surface of the nanoparticle aids in the initial binding to the cell wall, after which the nanoparticle is transported inside the cell by endocytosis or other transport phenomena. At some later time (typically 3 to 6 hours), the nanoparticles disintegrate, and the drug load is released into the cytoplasm. Due to the specificity of the drug spectral signature, the released drug can be identified. As few as thousand drug molecules can be detected by this methodology [103].

5. Conclusions

The previous sections described how IR and Raman spectroscopy can complement histopathology and reveal information that is available in classical methods only by costly and time-consuming steps such as IHC, PCR, gene array or other technologies. Due to the inherent sensitivity toward changes in the biomolecular composition of different cell and tissue types, vibrational spectroscopy can provide information that is superior to that of any one of the conventional techniques.

In this review, we summarized the present state-of-the-art of “molecular pathology” provided by vibrational micro-spectroscopy, and demonstrated that

- metastases could be identified in lymph nodes and brain tissue, and the primary tumor could be determined,
- the source of lymphocyte activation can be traced,
- different cancer types such as squamous cell carcinoma and adenocarcinoma can be distinguished without the use of morphological information,
- early stage abnormalities of oral and cervical mucosa cells can be detected and used for screening applications
- different cell types can be distinguished at the single cell level, which is extremely promising for the detection of circulating tumor cells
- events such as transport into cells can be monitored with exquisite sensitivity and specificity

The main difference compared to established methods is that no morphological information and no staining reagents are required, since IR and Raman spectra solely rely on molecular and biochemical features that can be probed in a non-destructive way.

What needs to be done next to transfer the vibrational spectroscopic approaches into clinical diagnosis? For the application of IR-SCP and IR-SHP into clinical laboratories, sophisticated FTIR imaging systems are available off the shelf and ready for use. Currently, research groups are working with medical collaborators to train classification models and validate them using a sufficiently large number of cases in retrospective studies. If these models are robust enough, they can be subjected to new cases to improve diagnosis and prognosis.

Raman imaging need further improvements to speed up data acquisition. Minimal sampling was suggested for rapid acquisitions of Raman images [104]. Raman signals can be enhanced in tissue or cells by surface enhanced Raman scattering (SERS) effect using functionalized metal nanoparticles [105–107] or by resonance Raman scattering probing prosthetic groups in chromophores [108]. Another promising signal enhancement approach constitutes non-linear, coherent Raman techniques such as coherent anti-Stokes Raman scattering (CARS) or stimulated Raman scattering [109]. CARS imaging offers video rate acquisition speed and enables detection of single cells and nuclei probing the CH-stretching wavenumber range [110]. Relevant histopathologic information such as nucleus to cytoplasm ratio, cell density, nucleus size and shape can be extracted from CARS images by innovative image processing procedures [111]. Compact and inexpensive fiber lasers for excitation with high energy and ultra-short pulses are under development. Once such instrumentation is readily available, large scale

datasets need to be acquired and classification models need to be trained as well. Furthermore, dedicated Raman fiber optic probes are required for real-time, *in vivo* applications. Such devices would even enable optical biopsies before and without surgery. Fiber-based Raman detection systems can also be incorporated in a microfluidic platform enabling alignment free devices for bioanalyte and cell sensing with minimal sample preparation [112].

Author biographies Please see Supporting Information online.

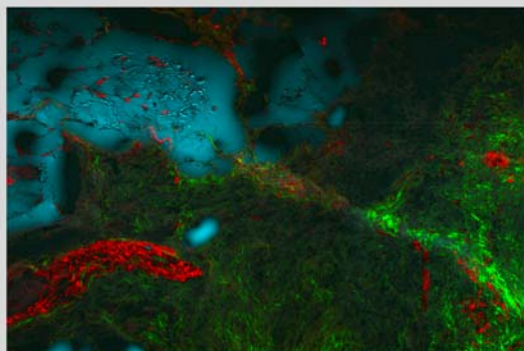
References

- [1] R. Virchow, *Vorlesungen über Pathologie* (Verlag von August Hirschwald, Berlin, 1871).
- [2] S. I. Hajdu, *Ann. Clin. Lab. Sci.* **35**, 203–205 (2005).
- [3] C. D. Sturgis, D. L. Nassar, J. A. D'Antonio, and S. S. Raab, *Am. J. Clin. Pathol.* **114**, 197–202 (2000).
- [4] G. Avwioro, *Pharm. Clinic. Sciences* **1**, 24–34 (2011).
- [5] E. Brachtel and Y. Yagi, *Journal of Biophotonics* **5**, 327–335 (2012).
- [6] L. Pantanowitz, P. N. Valenstein, A. J. Evans, K. J. Kaplan, J. D. Pfeifer, D. C. Wilbur, L. C. Collins, and T. J. Colgan, *J. Pathol. Inform.* **2**, 36–45 (2011).
- [7] A. H. Coons, H. J. Creech, R. N. Jones, and E. Berliner, *J. Immunol.* **45**, 159–170 (1942).
- [8] A. Stallmach, C. Schmidt, A. Watson, and R. Kieslich, *J. Biophotonics* **4**, 482–489 (2011).
- [9] W. Stummer, U. Pichlmeier, T. Meinel, O. D. Wiestler, F. Zanella, and H. J. Reulen, *Lancet Oncol.* **7**, 392–401 (2006).
- [10] J. Muller, A. Wunder, and K. Licha, *Recent Results Cancer Res.* **187**, 221–246 (2013).
- [11] M. Diem, S. Boydston-White, and L. Chiriboga, *App. Spectrosc.* **53**, 148A–161A (1999).
- [12] M. Diem, M. Romeo, S. Boydston-White, M. Miljkovic, and C. Matthäus, *Analyst* **129**, 880–885 (2004).
- [13] M. Diem, *Introduction to Modern Vibrational Spectroscopy* (Wiley-Interscience, New York, 1993).
- [14] J. Popp, V. V. Tuchin, A. Chiou, and S. H. Heinemann, *Handbook of Biophotonics, Vol. 1: Basics and Techniques* (Wiley-VCH, Weinheim, 2011).
- [15] M. Diem, P. R. Griffiths, and J. M. Chalmers, *Vibrational Spectroscopy for Medical Diagnosis* (John Wiley & Sons, Chichester, UK 2008).
- [16] S. Dochow, C. Krafft, U. Neugebauer, T. Bocklitz, T. Henkel, G. Mayer, J. Albert, and J. Popp, *Lab Chip* **11**, 1484–1490 (2011).
- [17] U. Neugebauer, T. Bocklitz, J. H. Clement, C. Krafft, and J. Popp, *Analyst* **135**, 3178–3182 (2010).
- [18] A. Barth, *Biochim. Biophys. Acta* **1767**, 1073–1101 (2007).
- [19] G. J. Thomas Jr., *Raman Spectroscopy of Biopolymers*, in: *Vibrational Spectra and Structure*, J. Durig (ed.) (Marcel Dekker, New York, 1975), pp. 239–315.
- [20] B. Prescott, W. Steinmetz, and G. J. Thomas Jr., *Biopolymers* **23**, 235–256 (1984).
- [21] M. J. Romeo, R. K. Dukor, and M. Diem, *Introduction to Spectral Imaging, and Applications to Diagnosis of Lymph Nodes* (John Wiley & Sons, Chichester, UK, 2008).
- [22] C. Matthäus, B. Bird, M. Miljković, T. Chernenko, M. J. Romeo, and M. Diem, *IR and Raman Microscopy in Cell Biology*, in: *Methods in Cell Biology*, Volume 89: Biophysical Tools for Biologists, Volume 2, edited by J. J. Correia and I. Detrich, H. W., Eds. (Elsevier, 2008), pp. 275–308.
- [23] J. M. Schubert, A. I. Mazur, B. Bird, M. Miljković, and M. Diem, *J. Biophotonics* **3**, 588–596 (2010).
- [24] M. Diem, M. Miljkovic, M. J. Romeo, B. Bird, J. Schubert, and K. Papamarkakis, *Method of Reconstituting Cellular Spectra Useful for Detecting Cellular Disorders*, in: *WO 2009/146425 A1 W. I. P. Organization* (ed.) (Northeastern University, 2009).
- [25] C. Krafft and R. Salzer, *Neurooncological Applications of IR and Raman Spectroscopy* (John Wiley & Sons, Chichester, UK, 2008).
- [26] C. Krafft, S. B. Sobottka, G. Schackert, and R. Salzer, *Raman Spectrosc.* **37**, 367–375 (2006).
- [27] C. Krafft, M. A. Diderhoshan, P. Recknagel, M. Miljković, M. Bauer, and J. Popp, *Vibr. Spectrosc.* **55**, 90–100 (2011).
- [28] Y. S. Huang, T. Karashima, M. Yamamoto, and H. Hamaguchi, *Biochemistry* **44**, 10009–10019 (2005).
- [29] M. Votteler, D. A. C. Berrio, M. Pudlas, H. Walles, U. A. Stock, and K. Schenke-Layland, *J. Biophotonics* **5**, 47–56 (2012).
- [30] H. Barr, C. Kendall, and N. Stone, *Photodiagnosis Photodyn. Ther.* **1**, 75–84 (2004).
- [31] H. Barr, C. Kendall, and N. Stone, *Raman Spectroscopy as a Potential Tool for Early Diagnosis of Malignancies in Esophageal and Bladder Tissues*, in: *Vibrational Spectroscopy for Medical Diagnosis* M. Diem, P. R. Griffiths and J. M. Chalmers (eds.) (John Wiley & Sons, Chichester, UK, 2008).
- [32] C. Kendall, J. Day, J. Hutchings, B. Smith, N. Shepherd, H. Barr, and N. Stone, *Analyst* **135**, 3038–3041 (2010).
- [33] L. M. Almond, J. Hutchings, N. Shepherd, H. Barr, N. Stone, and C. Kendall, *J. Biophotonics* **4**, 685–695 (2011).
- [34] C. Matthäus, T. Chernenko, J. A. Newmark, C. M. Warner, and M. Diem, *Biophys. J.* **93**, 668–673 (2007).
- [35] C. Matthäus, S. Boydston-White, M. Miljković, M. J. Romeo, and M. Diem, *Appl. Spectrosc.* **60**, 1–8 (2006).
- [36] E. Zuser, T. Chernenko, J. Newmark, M. Miljković and M. Diem, *Analyst* **136**, 3030–3033 (2010).
- [37] I. W. Schie, J. Wu, T. Weeks, M. A. Zern, J. C. Rutledge, and T. Huser, *J. Biophotonics* **4**, 425–434 (2011).
- [38] L. D. Chiu and H. O. Hamaguchi, *J. Biophotonics* **4**, 30–33 (2011).
- [39] L. D. Chiu, F. Hullin-Matsuda, T. Kobayashi, H. Torii and H. O. Hamaguchi, *J. Biophotonics* **5**, 724–728 (2012).

- [40] J. W. Chan, D. K. Lieu, T. Huser, and R. A. Li, *Anal. Chem.* **81**, 1324–1331 (2009).
- [41] S. O. Konorov, C. H. Glover, J. M. Piret, J. Bryan, G. Schulze, M. W. Blades, and R. F. B. Turner, *Anal. Chem.* **79**, 7221–7225 (2007).
- [42] I. Notingher, Label-free Imaging of Phenotypic Spectral Markers in Live Cells Derived from Human Stem Cells, in: 14th European Conference on the Spectroscopy of Biological Molecules (Coimbra University, Portugal, 2011).
- [43] A. Saha, R. Arora, V. V. Yakovlev, and J. M. Burke, *J. Biophotonics* **4**, 805–813 (2011).
- [44] M. Schmitt and J. Popp, *Chemie in unserer Zeit* **45**, 14–23 (2011).
- [45] H. Harz, M. Kiehntopf, S. Stöckel, P. Rösch, E. Straube, T. Deufel, and J. Popp, *J. Biophotonics* **2**, 70–80 (2009).
- [46] J. Filik, M. D. Frogley, J. K. Pijanka, K. Wehbe, and G. Cinque, *Analyst* **137**, 853–861 (2012).
- [47] A. I. Mazur, B. Bird, M. Miljković, and M. Diem, *J. Biophotonics* **6**, 101–109 (2013).
- [48] A. I. Mazur, E. J. Marcsisin, B. Bird, M. Miljković, and M. Diem, *Anal. Chem.* **84**, 1259–1266 (2012).
- [49] A. I. Mazur, E. J. Marcsisin, B. Bird, M. Miljković, and M. Diem, *Anal. Chem.* **84**, 8265–8271 (2012).
- [50] D. R. Whelan, K. R. Bambery, P. Heraud, M. J. Tobin, M. Diem, D. McNaughton, and B. R. Wood, *Nucleic Acids Res.* **39**, 5439–5448 (2011).
- [51] I. Notingher, I. Bisson, J. M. Polak, and L. L. Hench, *Vibr. Spectrosc.* **35**, 199–203 (2004).
- [52] M. Miljković, B. Bird, K. Lenau, A. I. Mazur, and M. Diem, *Analyst* **138**, 3975–3982 (2013).
- [53] E. Marcsisin, C. M. Uttero, A. I. Mazur, M. Miljković, B. Bird, and M. Diem, *Analyst* **136**, 2958–2964 (2012).
- [54] B. Mohlenhoff, M. J. Romeo, M. Diem, and B. R. Wood, *Biophys. J.* **88**, 3635–3640 (2005).
- [55] P. Bassan, A. Kohler, H. Martens, J. Lee, H. J. Byrne, P. Dumas, E. Gazi, M. Brown, N. Clarke, and P. Gardner, *Analyst* **135**, 268–277 (2010).
- [56] B. R. Wood, L. Chiriboga, H. Yee, M. Quinn, D. McNaughton, and M. Diem, *Gynec. Oncol.* **93**, 59–68 (2004).
- [57] M. A. Lavasani and F. Moynfar, *J. Biophotonics* **5**, 345–366 (2012).
- [58] M. J. Adams, *Chemometrics in Analytical Spectroscopy* (Royal Society of Chemistry, Cambridge, 2004).
- [59] J. M. P. Nascimento and J. M. Bioucas Dias, *IEEE Transactions Geoscience & Remote Sensing* **43**, 898–910 (2005).
- [60] M. E. Winter, *Proc. SPIE* **3753**, 266–275 (1999).
- [61] M. Miljković, T. Chernenko, M. J. Romeo, B. Bird, C. Matthäus, and M. Diem, *Analyst* **135**, 2002–2013 (2010).
- [62] M. Hedegaard, C. Matthäus, S. Hassing, C. Krafft, M. Diem, and J. Popp, *Theor. Chem. Acc.* **130**, 1249–1260 (2011).
- [63] P. Bassan, H. J. Byrne, F. Bonnier, J. Lee, P. Dumas, and P. Gardner, *Analyst* **134**, 1586–1593 (2009).
- [64] P. Bassan, H. J. Byrne, J. Lee, F. Bonnier, C. Clarke, P. Dumas, E. Gazi, M. D. Brown, N. W. Clarke, and P. Gardner, *Analyst* **134**, 1171–1175 (2009).
- [65] M. Miljković, B. Bird, and M. Diem, *Analyst* **137**, 3954–3964 (2012).
- [66] B. Bird, M. Miljković, and M. Diem, *J. Biophotonics* **3**, 597–608 (2010).
- [67] R. H. Schreiber, S. Pendas, N. N. Ku, D. S. Reintgen, A. R. Shons, C. Berman, D. Boulware, and C. E. Cox, *Ann. Surg. Oncol.* **6**, 95–101 (1999).
- [68] B. Bird, K. Bedrossian, N. Laver, M. Miljković, M. J. Romeo, and M. Diem, *Analyst* **134**, 1067–1076 (2009).
- [69] B. Bird, M. Miljković, N. Laver, and M. Diem, *Tech. Cancer Res. Treatment* **10**, 135–144 (2011).
- [70] B. Bird, M. J. Romeo, N. Laver, and M. Diem, *J. Biophotonics* **2**, 37–46 (2009).
- [71] C. Krafft, L. Shapoval, S. Sobottka, K. Geiger, G. Schakert, and R. Salzer, *Biochem. Biophys. Acta* **1758**, 883–891 (2006).
- [72] B. Bird, M. Miljković, S. Remiszewski, A. Akalin, M. Kon, and M. Diem, *Lab. Invest.* **92**, 1358–1373 (2012).
- [73] L. Hartsuiker, N. J. L. Zeijen, L. W. M. M. Terstappen, and C. Otto, *Analyst* **135**, 3220–3226 (2010).
- [74] G. A. Bishop, S. A. Haxhinasto, L. L. Stunz, and B. S. Hostager, *Crit. Rev. Immunology* **23**, 165–213 (2003).
- [75] D. Helm, H. Labischinski, G. Schallen, and D. Naumann, *J. Gen. Microbiol.* **137**, 69–79 (1991).
- [76] M. K. Bijsterbosch, C. J. Meade, G. A. Turner, and G. G. B. Klaus, *Cell* **41**, 999–1006 (1985).
- [77] A. Kallenbach-Thieltges, F. Grosseruschkamp, A. Mosig, M. Diem, A. Tannapfel, and K. Gerwert, *J. Biophotonics* **6**, 88–100 (2013).
- [78] P. Wong, R. Wong, T. Caputo, T. Godwin, and B. Rigas, *Proc. Natl. Acad. Sci.* **88**, 10988–10992 (1991).
- [79] M. Fung, K. Fung, M. Senterman, P. Eid, W. Faught, N. Mikhael, and P. T. T. Wong, *Gynecol. Oncol.* **66**, 10–15 (1997).
- [80] P. T. T. Wong, R. Wong, and M. F. K. Fung, *App. Spectrosc.* **47**, 1058–1063 (1993).
- [81] M. Cohenford and B. Rigas, *Proc. Natl. Acad. Sci.* **95**, 15327–15332 (1998).
- [82] M. Diem, C. Matthäus, T. Chernenko, M. J. Romeo, M. Miljković, B. Bird, J. Schubert, K. Papamarkakis, K. Bedrossian, and N. Laver, *IR and Raman Spectroscopy and Spectral Imaging of Individual Cells*, in: *IR and Raman Spectroscopic Imaging*, R. Salzer and H. W. Siesler (eds.) (Wiley-VCH Publishing, Weinheim, Germany, 2009), pp. 173–202.
- [83] J. M. Schubert, B. Bird, K. Papamarkakis, M. Miljković, K. Bedrossian, N. Laver, and M. Diem, *Lab. Invest.* **90**, 1068–1077 (2010).
- [84] K. Papamarkakis, B. Bird, J. M. Schubert, M. Miljković, R. Wein, K. Bedrossian, N. Laver, and M. Diem, *Lab. Invest.* **90**, 589–598 (2010).
- [85] J. M. Schubert, *Spectral Cytology of Human Oral and Cervical Samples*, in: *Chemistry & Chemical Biology* (Northeastern University, Boston, 2011).

- [86] K. Ostrowska, *Vibrational Spectroscopy for Cervical Cytology*, in: School of Physics, Dublin (Institute of Technology, Dublin, 2011).
- [87] K. M. Tan, C. S. Herrington, and C. T. A. Brown, *J. Biophotonics* **4**, 40–48 (2011).
- [88] K. S. Polyzoidis, G. Miliaras, and N. Pavlidis, *Cancer Treat. Rev.* **31**, 247–255 (2005).
- [89] C. Krafft, L. Shapoval, S. B. Sobottka, G. Schackert, and R. Salzer, *Tech. Cancer Res. Treatment* **5**, 1–8 (2006).
- [90] C. Krafft, M. Kirsch, C. Beleites, G. Schackert, and R. Salzer, *Anal. Bioanal. Chem.* **389**, 1133–1142 (2007).
- [91] M. Kirsch, G. Schackert, R. Salzer, and C. Krafft, *Anal. Bioanal. Chem.* **398**, 1707–1713 (2010).
- [92] N. Bergner, T. Bocklitz, B. F. M. Romeike, R. Reichart, R. Kalff, C. Krafft, and J. Popp, *Chemom. Intell. Lab. Syst.* **117**, 224–232 (2012).
- [93] T. Meyer, N. Bergner, C. Bielecki, C. Krafft, D. Aki-mov, B. F. Romeike, R. Reichart, R. Kalff, B. Dietzek, and J. Popp, *J. Biomed. Opt.* **16**, 021113 (2011).
- [94] C. Krafft, B. Dietzek, M. Schmitt, and J. Popp, *J. Biomed. Opt.* **17**, 040801 (2012).
- [95] U. Neugebauer, J. H. Clement, T. Bocklitz, C. Krafft, and J. Popp, *J. Biophotonics* **3**, 579–587 (2010).
- [96] J. W. Chan, *J. Biophotonics* **6**, 36–48 (2013).
- [97] P. R. T. Jess, V. Garces-Chavez, D. Smith, M. Mazilu, L. Paterson, A. Riches, C. S. Herrington, W. Sibbett, and K. Dholakia, *Opt. Express* **14**, 5779–5791 (2006).
- [98] A. Y. Lau, L. P. Lee, and J. W. Chan, *Lab. Chip* **8**, 1116–1120 (2008).
- [99] M. J. Romeo, S. Boydston-White, C. Matthäus, M. Miljković, B. Bird, T. Chernenko, P. Lasch, and M. Diem, *IR and Raman Microspectroscopic Studies of Individual Human Cells* (John Wiley & Sons, Chichester, UK, 2008).
- [100] C. Matthäus, T. Chernenko, L. Quintero, L. Milane, A. Kale, M. Amiji, V. Torchilin, and M. Diem, *Proc. SPIE* **6991**, 101–108 (2008).
- [101] T. Chernenko, C. Matthäus, L. Milane, L. Quintero, M. Amiji, and M. Diem, *ACS Nano* **3**, 3552–3558 (2009).
- [102] T. Chernenko, *Non-invasive and label-free imaging of sub-cellular architecture and nano-drug delivery carriers using Raman micro-spectroscopy*, in: Department of Chemistry and Chemical Biology (Northeastern University, Boston, 2010).
- [103] H.-J. van Manen, Y. M. Kraan, D. Ross, and C. Otto, *Proc Natl Acad Sci* **102**, 10159–10164 (2005).
- [104] C. J. Rowlands, S. Varma, W. Perkins, I. Leach, H. Williams, and I. Nottingher, *J. Biophotonics* **5**, 220–229 (2012).
- [105] K. W. Kho, C. Y. Fu, U. S. Dinis, and M. Olivo, *J. Biophotonics* **4**, 667–684 (2011).
- [106] M. Sauer, D. Graham, and P. Tinnefeld, *J. Biophotonics* **4**, 375–376 (2011).
- [107] M. Schütz, C. I. Müller, M. Salehi, C. Lambert, and S. Schlücker, *J. Biophotonics* **4**, 453–463 (2011).
- [108] M. Kakita, V. Kaliaperumal, and H.-O. Hamaguchi, *J. Biophotonics* **5**, 20–24 (2012).
- [109] J. L. Suhaim, J. C. Boik, B. J. Tromberg, and E. O. Potma, *J. Biophotonics* **5**, 387–395 (2012).
- [110] T. Meyer, N. Bergner, A. Medyukhina, B. Dietzek, C. Krafft, B. F. M. Romeike, R. Reichart, R. Kalff and J. Popp, *J. Biophotonics* **5**, 729–733 (2012).
- [111] A. Medyukhina, T. Meyer, M. Schmitt, B. F. M. Romeike, B. Dietzek, and J. Popp, *J. Biophotonics* **5**, 878–888 (2012).
- [112] P. C. Ashok, A. C. De Luca, M. Mazilu, and K. Dholakia, *J. Biophotonics* **4**, 514–518 (2011).

+++ COMING SOON +++ COMING SOON +++ COMING SOON +++



2013. approx. 272 Pages, Hardcover
approx. 62 figures (12 color figs.)
978-3-527-33513-8

JÜRGEN POPP, Jena, Germany (ed.)

Ex-vivo and In-vivo Optical Molecular Pathology

The result of a unique collaboration between clinicians and physicists, this book provides an unparalleled overview of a new generation of diagnostic tools in clinical pathology. The input from both physicists developing new methods as well as routine clinicians familiar with practical aspects and medical relevance guarantees that this practical work is a valuable asset for a wide audience, including technical personnel and decision makers in treatment centers, experts working in companies developing diagnostic devices, and clinicians specializing in advanced diagnostic methods. Since basic researchers are increasingly adopting novel diagnostic tools developed for human use as well, this will also be of interest for biomedical research institutions with large animal facilities.

Register now for the free
WILEY-VCH Newsletter!
www.wiley-vch.de/home/pas

WILEY-VCH • P.O. Box 10 11 61 • 69451 Weinheim, Germany
Fax: +49 (0) 62 01 - 60 61 84
e-mail: service@wiley-vch.de • <http://www.wiley-vch.de>

WILEY-VCH